Published in final edited form as:
J Am Chem Soc. 2008 November 19; 130(46): 15448–15459. doi:10.1021/ja804339m.

Defining the Electronic and Geometric Structure of One-Electron Oxidized Copper–Bis-phenoxide Complexes

Tim Storr[†], **Pratik Verma**[†], **Russell C. Pratt**[†], **Erik C. Wasinger**[*,‡], **Yuichi Shimazaki**[*,§], and **T. Daniel P. Stack**[*,†]

Department of Chemistry, Stanford University, Stanford, California 94305, Department of Chemistry and Biochemistry, California State University, Chico, California 95929, and College of Science, Ibaraki University, Bunkyo, Mito 310-8512, Japan

Abstract

The geometric and electronic structure of an oxidized Cu complex ([Cu**Sal**]$^+$; **Sal** = *N*, *N*′-bis(3,5-di-*tert*-butylsalicylidene)-1,2-cyclohexane-(1*R*,2*R*)-diamine) with a non-innocent salen ligand has been investigated both in the solid state and in solution. Integration of information from UV–vis–NIR spectroscopy, magnetic susceptibility, electrochemistry, resonance Raman spectroscopy, X-ray crystallography, X-ray absorption spectroscopy, and density functional theory calculations provides critical insights into the nature of the localization/delocalization of the oxidation locus. In contrast to the analogous Ni derivative [Ni**Sal**]$^+$ (Storr, T.; et al. *Angew. Chem., Int. Ed.* **2007**, *46*, 5198), which exists solely in the Ni(II) ligand-radical form, the locus of oxidation is metal-based for [Cu**Sal**]$^+$, affording exclusively a Cu(III) species in the solid state (4–300 K). Variable-temperature solution studies suggest that [Cu**Sal**]$^+$ exists in a reversible spin-equilibrium between a ligand-radical species [Cu(II)**Sal**$^\bullet$]$^+$ ($S = 1$) and the high-valent metal form [Cu(III)**Sal**]$^+$ ($S = 0$), indicative of nearly isoenergetic species. It is surprising that a bis-imine–bis-phenolate ligation stabilizes the Cu(III) oxidation state, and even more surprising that in solution a spin equilibrium occurs without a change in coordination number. The oxidized tetrahydrosalen analogue [Cu**Sal**$^{\mathbf{red}}$]$^+$ (**Sal**$^{\mathbf{red}}$ = *N*, *N*′-bis(3,5-di-*tert*-butylhydroxybenzyl)-1,2-cyclohexane-(1*R*,2*R*)-diamine) exists as a temperature-invariant Cu(II)–ligand-radical complex in solution, demonstrating that ostensibly simple variations of the ligand structure affect the locus of oxidation in Cu–bis-phenoxide complexes.

1. Introduction

The interplay of redox-active transition metal ions and pro-radical ligands in metalloenzyme sites is an area of considerable research interest.[1] Galactose oxidase (GOase) is the archetypical example,[2] catalyzing the aerobic oxidation of primary alcohols to aldehydes via two one-electron cofactors: a copper atom and a cysteine-modified tyrosine residue. The consensus mechanism involves an oxidized form ($GOase_{ox}$) that contains a Cu(II)-tyrosine radical, which binds the alcoholic substrate in an exchangeable equatorial position (Scheme 1). Subsequent

E-mail: ewasinger@csuchico.edu; yshima@mx.ibaraki.ac.jp; stack@stanford.edu.
[†]Stanford University.
[‡]Chico State University.
[§]Ibaraki University.

Supporting Information Available: Complete ref [80]; experimental details including the CIF file for the X-ray structure of [Cu**Sal**]$^+SbF_6^-$, solid-state magnetic data for Cu**Sal** and [Cu**Sal**]$^+SbF_6^-$, Cu L-edge XAS photoreduction plots for [Cu**Sal**]$^+$ and [PPh_4][Cu-*N*, *N*′-*o*-phenylene-bis(methylamide)], EXAFS fit results for Cu**Sal** and [Cu**Sal**]$^+$, VT ^{1}H NMR of [Cu**Sal**]$^+SbF_6^-$, concentration-dependent UV–vis studies on [Cu**Sal**]$^+SbF_6^-$, and VT solution susceptibility and absorption spectroscopy for [Cu**Sal**$^{\mathbf{red}}$]$^+$; computational details including the [Cu**Sal**]$^+$ triplet spin density, TD-DFT excitation energies and oscillator strengths, orbital constituent analysis, and the Cartesian coordinates for the geometry-optimized Cu**Sal**, [Cu-**Sal**]$^+$ (singlet), and [Cu**Sal**]$^+$ (triplet) species. This material is available free of charge via the Internet at http://pubs.acs.org.

hydrogen atom abstraction and electron transfer lead to the formation of the aldehyde product and the reduced form of the enzyme ($GOase_{red}$). Due to the apparent simplicity of the GOase active site, and the importance of selective and "green" alcohol oxidation catalysts, much effort has been devoted to the synthesis of structural and functional small-molecule models of this enzyme.[3–8] This research has led to an improved understanding of the interaction between transition metals and non-innocent ligands.[9–12]

We have focused our efforts on the copper–bis-phenoxide complexes Cu**Sal** and Cu$\mathbf{Sal}^{\mathbf{red}}$ (Scheme 2) as small-molecule GOase models.[3,4] These two square-planar complexes are structurally similar; however, the phenolates of the reduced derivative (Cu$\mathbf{Sal}^{\mathbf{red}}$) are more basic due to reduction of the imine functions. The one-electron oxidized forms [Cu**Sal**]$^+$ and [Cu$\mathbf{Sal}^{\mathbf{red}}$]$^+$ display interesting NIR features (CH_2Cl_2; [Cu**Sal**]$^+$, 5700 cm^{-1}; [Cu$\mathbf{Sal}^{\mathbf{red}}$]$^+$, 6250 cm^{-1})[3] and act as stoichiometric oxidants of benzyl alcohol yielding benzaldehyde, mimicking the substrate oxidizing half-reaction of GOase. Interestingly, [Cu$\mathbf{Sal}^{\mathbf{red}}$]$^+$ reacts approximately 10 times faster as compared to [Cu**Sal**]$^+$, even though [Cu$\mathbf{Sal}^{\mathbf{red}}$]$^+$ is a significantly weaker oxidant (CH_2Cl_2, ΔE_{ox} = 370 mV).[3] Kinetic studies suggest that the enhanced reactivity of [Cu$\mathbf{Sal}^{\mathbf{red}}$]$^+$ is due to a substrate binding equilibrium process, analogous to substrate binding steps observed for many enzymes, including GOase; [Cu**Sal**]$^+$ by contrast reacts by a simple bimolecular rate-limiting step. In this work, we have further investigated the electronic structure of [Cu**Sal**]$^+$ and [Cu$\mathbf{Sal}^{\mathbf{red}}$]$^+$ in order to gain insight into this differential reactivity.

Tetradentate salen ligands (salen is a common abbreviation for N_2O_2 bis-Schiff-base bis-phenolate ligands), and their reduced tetrahydrosalen analogues, have received considerable attention as ligand systems due to their relative ease of synthesis, ability to form stable complexes with many metals in a variety of oxidation states, similarity of ligating groups found in metalloproteins and enzymes, and versatility as catalysts for important organic transformations.[13] Without the use of *ortho* and *para* phenolate protecting groups to prevent radical coupling, oxidized metal–salen complexes are prone to rapid polymerization, restricting study of the oxidized species.[14] More recent work has focused on investigating the electronic structure of suitably protected oxidized metal salens and tetrahydrosalens, determining the factors that control the locus of oxidation in these complexes.[6,15–20] Insight from this and other work[21] has led to the recent development of small-molecule systems that exploit ligand non-innocence for catalytic applications.[22]

Depending on the relative energies of the redox-active orbitals, metal complexes with pro-radical ligands can exist in one of two limiting descriptions: a metal–ligand-radical ($M^{n+}(L^{\bullet})$) or a high-valent metal complex ($M(^{n+1)+}(L^{-})$). In the absence of exogenous ligands, oxidized Ni salens exist in the ligand-radical form, and we have recently characterized [Ni**Sal**]$^+SbF_6^-$ in the solid state.[18] In the presence of coordinating counterions and/or solvent, the complex exists as a high-valent Ni(III) complex, [Ni**Sal**$(L)_2]^+$, revealing that modulation of the ligand field via axial ligand binding can shift the locus of oxidation within the complex. We have now investigated the electronic structure of the analogous [Cu**Sal**]$^+$ derivative, which could also potentially exist in either a ligand-radical or high-valent metal form. Due to the specific geometric preferences of Ni and Cu, the factors governing the locus of oxidation differ. While Ni(III) d^7 complexes are stabilized generally in an octahedral environment, a compact square-planar ligand geometry is much preferred for Cu(III) d^8 complexes.[23] Indeed, the majority of reported Cu(III) complexes are four-coordinate and employ a combination of polarizable anionic ligands such as carboxylates,[24] thiolates,[25] deprotonated amides,[26–28] carbamates,[29] and N-confused porphyrins.[30] Only a small number of nonplanar Cu(III) complexes have been reported.[31] Recent interest in the stabilization of the Cu(III) oxidation state stems from the synthesis and reactivity of bis(μ-oxo)dicopper(III) complexes[32,33] and the isolation of Cu

(III) intermediates in organocopper chemistry[34] as well as in a functional tyrosinase model system.[35]

While the salen ligand system provides a dianionic square-planar environment capable of stabilizing a Cu(III) oxidation state, the lack of sufficient anionic and highly polarizable donor groups is thought to preclude access to this metal oxidation state. By a combination of experiments and calculations, we now show that [Cu**Sal**]$^+$ exists as a Cu(III) complex in the solid state at 300 K, yet is involved in a temperature-dependent equilibrium between ligand-radical and high-valent metal forms in solution, demonstrating the nearly isoenergetic nature of these two electronic states.

2. Results and Analysis

2.1. Synthesis and Solid-State Characterization of [Cu-Sal]$^+$SbF$_6^-$

2.1.1. Synthesis and Solid-State Structure of [Cu-Sal]$^+$SbF$_6^-$—Oxidation of Cu**Sal** to [Cu**Sal**]$^+$SbF$_6^-$ was completed with either $AgSbF_6$ ($E_{1/2}$ = +650 mV vs Fc/Fc$^+$) or thianthrenyl (Th$^{+\bullet}$) hexafluoroantimonate ($E_{1/2}$ = +890 mV vs Fc/Fc$^+$) in CH_2Cl_2.[36] The resulting purple-colored solution is stable for days at room temperature in the absence of O_2 and/or H_2O. Oxidation with $AgSbF_6$ allows for clean isolation of the oxidized complex, free of oxidant byproduct. Indeed, single crystals of [Cu**Sal**]$^+$SbF$_6^-$ suitable for X-ray structural analysis were isolated by vapor diffusion of pentane into a concentrated CH_2Cl_2 solution of the complex prepared in this manner. The molecular structure of [Cu**Sal**]$^+$SbF$_6^-$ is shown in Figure 1, and selected crystallographic data are presented in Table 1.

The angle between the N(1)–Cu(1)–O(1) and N(2)–Cu(1)–O(2) planes in [Cu**Sal**]$^+$ is 4.7°, substantially reduced from the value of 19.8° for the distorted square-planar Cu**Sal**.[37] A weak axial Cu–F interaction (2.76 Å) exists between the counterion and the metal center in [Cu**Sal**]$^+$. Comparison of the metal–ligand bond lengths for Cu**Sal** and [Cu**Sal**]$^+$ shows that the coordination sphere is contracted in the oxidized complex (Table 2); on average the Cu–O and Cu–N bond lengths decrease by 0.04 and 0.03 Å respectively upon oxidation. This result is in contrast to the majority of reported metal–phenoxyl-radical complexes, in which the metal–phenoxyl bond lengthens, consistent with a reduction of the electron-donating ability of a phenoxyl ligand as compared to a phenolate.[8,38] Oxidation of the metal center to Cu(III), resulting in a decreased ionic radius for Cu and a gain in ligand-field stabilization energy, could explain the observed coordination sphere contraction for [Cu**Sal**]$^+$.[24–26,39] The more rigorously square-planar structure for [Cu**Sal**]$^+$, as compared to Cu**Sal**, also supports this conclusion.

2.1.2. Theoretical Characterization—Density functional theory (DFT) calculations on Cu**Sal** and [Cu**Sal**]$^+$ well reproduce the coordination sphere bond lengths including the coordination sphere contraction upon oxidation. At the B3LYP[40]/6–31g(d) level of theory for all atoms, the Cu coordination distances predicted by geometry optimization of Cu**Sal** and [Cu**Sal**]$^+$ ([Cu(III)**Sal**]$^+$; singlet) match those of the X-ray structures within ±0.02 Å (Table 2). The coordination sphere contraction is consistent with the increased Mayer bond order[41] (2.7–3.2) between the Cu and the ligand fragments upon oxidation, signifying enhanced covalency in the oxidized form. Broken symmetry (BS) optimizations for [Cu**Sal**]$^+$ collapsed to a singlet solution in all cases, suggesting that the [Cu(III)**Sal**]$^+$ state is electronically lower in energy than the anti-ferromagnetically coupled [Cu(II)**Sal**$^\bullet$]$^+$ state. Optimization of [Cu**Sal**]$^+$ as a triplet ([Cu(II)**Sal**$^\bullet$]$^+$) predicts a small increase in Mayer bond order (from 2.7 to 2.8) and an expanded coordination sphere in comparison to the experimental bond lengths for [Cu**Sal**]$^+$ (Table 2).

In order to better interpret the bonding changes upon oxidation, the *change* in electron donation between the metal and ligand fragments upon oxidation was analyzed using an extended charge decomposition analysis (ECDA) (Table 3).[42–44] In this ECDA analysis, the ligand-to-metal (L→M) electron donation is quantified by the contribution of the occupied fragment orbitals (OFOs) of the dianionic ligand to the unoccupied molecular orbitals (UMOs) of the complex.[45] Conversely, the metal-to-ligand (M→L) electron donation is quantified by the percentage of the unoccupied fragment orbitals (UFOs) of the ligand to the occupied molecular orbitals (OMOs) of the complex. ECDA analysis of both Cu**Sal** and [Cu(III)**Sal**]$^+$ shows that the overall electron donation from the ligand to Cu increases by ca. 2.2 electrons upon oxidation, consistent with the increased Mayer bond order calculated for [Cu(III)**Sal**]$^+$. Although both donation (L→Cu) and back-donation (Cu→L) increase for [Cu(III)**Sal**]$^+$, the former dominates, comprising ca. 85% of the |change| as shown in Table 3. In contrast to the analysis for [Cu(III)**Sal**]$^+$, evaluation of the bonding for the DFT-optimized triplet species [Cu(II)**Sal**$^\bullet$]$^+$ shows that both donation (L→Cu) and back-donation (Cu→L) increase by similar values upon oxidation to [Cu(II)**Sal**$^\bullet$]$^+$, such that the net electron donation remains effectively unchanged. ECDA analysis of Ni**Sal** and the one-electron oxidized ligand–radical complex, [Ni(II)**Sal**$^\bullet$]$^+$,[18] allows for a comparison of the electronic structure and bonding changes upon oxidation for both the Ni and Cu derivatives. Evaluation of the bonding for Ni**Sal** and the experimentally characterized ligand-radical complex, [Ni(II)**Sal**$^\bullet$]$^+$,[18] matches well with the analysis for [Cu(II)**Sal**$^\bullet$]$^+$, but not for [Cu(III)**Sal**]$^+$, and highlights the differences in bonding associated with metal-based as opposed to ligand-based oxidation in these systems.

2.1.3. Magnetic Properties—The temperature-dependent magnetic susceptibility of Cu**Sal** displays a response typical for a simple d^9 Cu(II) paramagnet, and the data were fit to a Curie–Weiss law expression ($C = 0.405$, $\theta = -0.554$ K; Figure S1).[48] The data for a powdered crystalline sample of [Cu**Sal**]$^+SbF_6^-$ show that this sample is essentially diamagnetic (μ_{eff} = 0.3 μ_B) in the temperature range 5–300 K.[48] The [Cu**Sal**]$^+SbF_6^-$ data were fit with a ca. 4% Cu**Sal** impurity, estimated from the low-temperature data, consistent with a small amount of decomposition in the solid-state sample. These results suggest that [Cu**Sal**]$^+SbF_6^-$ in the solid state has a diamagnetic electronic ground state ($S = 0$) with no thermally accessible triplet state at 300 K.

2.1.4. Cu K-Edge X-ray Absorption Spectroscopy (XAS)—Cu K-edge XAS was used to probe the metal oxidation state and structure of Cu**Sal** and [Cu**Sal**]$^+$ in the solid state. The Cu K-edge data for Cu**Sal** and [Cu**Sal**]$^+$ (Figure 2) show distinct differences, attributable to a change in metal oxidation state from Cu(II) to Cu(III) upon oxidation. The Cu K-edge 1s→3d transition, or pre-edge, is a successful indicator of copper oxidation state,[33,46] and the shift in the energy of the pre-edge feature from 8979.2 eV for Cu**Sal** to 8980.2 eV for [Cu**Sal**]$^+$ (Table 4) is consistent with a change in metal oxidation state from Cu(II) to Cu(III). The increased intensity of the 1s→3d transition for Cu**Sal**, as compared to [Cu**Sal**]$^+$, suggests greater distortion from a square-planar geometry for the former; the dipole-forbidden, quadrupole-allowed 1s→3d transition gains intensity through 4p mixing into the 3d orbitals.[47]

Extended X-ray absorption fine structure (EXAFS) data and representative fits for Cu**Sal** and [Cu**Sal**]$^+$ are shown in Figure 3. For Cu**Sal**, the four N/O donors[49] of the salen ligand were fit with a single shell at a distance of 1.90 Å, comparing very well with the average X-ray and computational data in Table 2. Additionally, two parameters were required to fit the outer shell contributions to the EXAFS data: a shell of single scattering carbon atoms at 2.87 Å and multiple scattering from the same carbons at 3.12 Å. Only two contributions were needed to fit the EXAFS data for [Cu**Sal**]$^+$. The Cu–N/O first shell distance was fit at 1.86 Å, which corresponds closely with the average of the X-ray data (Table 2), highlighting the coordination

sphere contraction upon oxidation. In addition, a carbon single scattering wave was fit at 2.83 Å.

2.1.5. Cu L-Edge XAS—Due to the low intensities of the Cu K-edge pre-edge features,[47] Cu L-edge XAS was investigated, as the associated $2p \rightarrow 3d_{x^2-y^2}$ transitions are electric-dipole-allowed and typically result in well-resolved peaks.[50,51] Similarly to the Cu K-pre-edge position, the energies of the L-edge transitions are sensitive to the metal oxidation state. The Cu L-edge XAS data for Cu**Sal**, [Cu**Sal**]$^+$, and the Cu(III) oxide $La_2Li_{0.5}Cu_{0.5}O_4$[52] (Figure 4) exhibit two major features, corresponding to the L_3-edge (ca. 930 eV, $2p_{3/2} \rightarrow 3d_{x^2-y^2}$) and the L_2-edge (ca. 950 eV, $2p_{1/2} \rightarrow 3d_{x^2-y^2}$).[53] The L_3-edge for Cu**Sal** occurs at 931.6 eV, which compares well with the data for $[CuCl_4]^{2-}$ (Table 5).

Interestingly, two features are observed for each of the L_3-and L_2-edges of [Cu**Sal**]$^+$. For the L_3-edge, peaks at 931.8 and 933.1 eV are visible, due to the presence of both a Cu(II) and a Cu(III) species in the sample. Corresponding peaks at 951.8 and 953.2 eV are present at the L_2-edge. The higher energy peaks for [Cu**Sal**]$^+$ correspond well with the Cu(III) oxide $La_2Li_{0.5}Cu_{0.5}O_4$ spectrum and are consistent with the presence of a Cu(III) species.[53] The presence of peaks indicative of a Cu(II) species in the spectrum of [Cu**Sal**]$^+$ is due to sample photoreduction, as continued exposure of a sample of [Cu**Sal**]$^+$ to the X-ray beam over 9 h leads to complete photoreduction to a Cu(II) species (Figure S2).[48] L-edge XAS of a very stable Cu(III)–oxamide complex,[26] $[PPh_4]$[Cu-*N*, *N*′-*o*-phenylene-bis-(methylamide)], also exhibited facile photoreduction under these experimental conditions (Figure S3).[48]

2.1.6. Cu X-ray Photoelectron Spectroscopy (XPS)—Cu XPS of solid Cu**Sal** and [Cu**Sal**]$^+$ shows a clean shift in the Cu $2p_{3/2}$ and Cu $2p_{1/2}$ binding energies to higher energy for the one-electron oxidized form (Figure 5). The 1.2 eV shift in the Cu $2p_{3/2}$ (933.7 to 934.9 eV) and Cu $2p_{1/2}$ (953.7 to 954.9 eV) binding energies is consistent with a change in oxidation state from Cu(II) for Cu**Sal** to Cu(III) for [Cu**Sal**]$^+$ and compares well with the magnitude and direction of the change in the Cu K-pre-edge energy for the same compounds (Table 4). The lower intensity beam used for the XPS experiments limits sample photoreduction in comparison to the L-edge XAS data (*vide supra*).

2.2. Characterization of [CuSal]$^+$ in Solution

2.2.1. Absorption Spectroscopy—The electronic spectrum of Cu**Sal** (Figure 6) is typical of a Cu(II) d^9 complex with an intense CT transition at 26 000 cm^{-1} (ε = 11 600 M^{-1} cm^{-1}) and a weak d–d transition at 17 600 cm^{-1} (ε = 600 M^{-1} cm^{-1}).[3,6] As reported previously, oxidation to [Cu**Sal**]$^+$ at room temperature results in the appearance of two new bands: an intense band at 18 000 cm^{-1} (ε = 6500 M^{-1} cm^{-1}) and a low-energy transition at 5700 cm^{-1} (ε = 2900 M^{-1} cm^{-1}).[3] Interestingly, the 18 000 cm^{-1} band exhibits large intensity changes with temperature (Figure 6). From 298 to 190 K, the 18 000 cm^{-1} band approximately doubles in intensity and shifts slightly to higher energy. This change is fully reversible and indicates that [Cu**Sal**]$^+$ is involved in a temperature-dependent equilibrium in solution. The intensity of the 18 000 cm^{-1} absorption band for [Cu**Sal**]$^+SbF_6^-$ is independent of concentration at both 295 and 203 K (Figures S4 and S5),[48] excluding dimerization as a possible reason for the observed temperature-dependent changes in band intensity.

2.2.2. Theoretical Analysis of the Electronic Transitions for [CuSal]$^+$—In order to better understand the electronic structure of [Cu**Sal**]$^+$, the nature of the transitions at 18 000 and 5700 cm^{-1} were investigated by time-dependent density functional theory (TD-DFT).[54] The calculated spectrum[55] for a [Cu(III)**Sal**]$^+$ singlet electronic ground state (Figure 6) agrees remarkably well with experiment in the visible and NIR regions. The predicted band at 18 600 cm^{-1} is predominantly a βHOMO-4 → βLUMO transition (Figure 7, Table 6). Analysis of the

compositions of the MOs (Figure 7; Table S2)[48] leads to an assignment of this band as a ligand-to-metal charge-transfer (LMCT) transition; orbital analysis shows that significant electron density is transferred from the phenolate oxygen atoms to the empty Cu $d_{x^2-y^2}$ orbital of the LUMO.[42,43]

The low-energy band (βHOMO → βLUMO) is also predicted to be a LMCT transition with an even more substantial change in Cu character (4 to 30%). A LMCT transition at a similar low energy (4200 cm^{-1}) has been characterized for a copper–superoxo complex.[56] Interestingly, the energies of the calculated transitions for the triplet [Cu(II)**Sal**$^{\bullet}$]$^+$ correspond closely to that for the singlet state (Table 6). The longer coordination sphere bond lengths for the triplet state, reflecting lesser covalency, leads to the slight red-shift of the predicted visible band in comparison to the singlet results. Both the singlet and triplet calculations predict the existence of a NIR band for [Cu**Sal**]$^+$; however, the NIR band for the triplet state is predicted to be a ligand-to-ligand charge-transfer (LLCT) transition on the basis of MO constituent analysis (Table S2).

2.2.3. Resonance Raman (rR) Spectroscopy—Resonance Ra-man spectroscopy is an important tool for the characterization of phenoxyl radical species.[11] Excitation in resonance with the phenoxyl $\pi \rightarrow \pi^*$ transition (ca. 400 nm) leads to the appearance of characteristic bands at ~1500 (ν_{7a}, C–O stretching) and ~1600 cm^{-1} (ν_{8a}, C_{ortho}–C_{meta} stretching).[7,57] As an example for the salen ligand framework, [Ni**Sal**]$^+$ exhibits bands at 1504 and 1605 cm^{-1} with 413 nm irradiation, consistent with a phenoxyl radical species ([Ni(II)**Sal**$^{\bullet}$]$^+$).[16] The rR spectrum of Cu**Sal** (Figure 8a) displays phenolate bands at 1528 and 1638 cm^{-1}.[16,58] No evidence for a phenoxyl radical species was provided by the rR spectrum of [Cu**Sal**]$^+$ (Figure 8b), as the bands observed at 1530 and 1598 cm^{-1} do not correlate with the expected pattern for a phenoxyl radical species. Comparison of the rR spectra for Cu**Sal**$^{\mathbf{red}}$ (Figure 8c) and [Cu**Sal**$^{\mathbf{red}}$]$^+$ (Figure 8d) shows that two new bands at 1495 and 1597 cm^{-1} are present upon oxidation. The energy of these two bands, and the frequency difference between them, signify the formation of a Cu(II) phenoxyl-radical species ([Cu(II)**Sal**$^{\bullet\mathbf{red}}$]$^+$). The presence of both phenoxyl and phenolate bands for [Cu**Sal**$^{\mathbf{red}}$]$^+$ may indicate localization of the phenoxyl radical on one of the two phenolates on the time scale of the Raman experiment.[17,59] It is interesting that the absorption spectra of the ligand-radical derivatives [Ni(II)**Sal**$^{\bullet}$]$^+$ and [Cu(II)**Sal**$^{\bullet\mathbf{red}}$]$^+$ lack definitive phenoxyl absorption bands at ca. 400 nm.[3,16]

2.2.4. Variable-Temperature (VT) ^{1}H NMR Spectroscopy—The ^{1}H NMR spectrum of [Cu**Sal**]$^+SbF_6^-$ in CD_2Cl_2 at 298 K displays broad signals over a wide spectral range (Figure S6),[48] indicating the presence of a substantial amount of a paramagnetic species. Solution susceptibility measurements by the Evans method[60] indicate a $\chi_m T$ value of 0.442 cm^3 mol^{-1} K (1.1 ± 0.1 unpaired electrons; spin-only calculation) at room temperature. An interpretation of this bulk susceptibility is the presence of approximately equimolar ferromagnetically coupled Cu(II)–ligand-radical species [Cu(II)**Sal**$^{\bullet}$]$^+$ and a diamagnetic counterpart [Cu(III)**Sal**]$^+$ (Figure 9).

Interestingly, as the temperature is decreased, the solution becomes less paramagnetic: the signals sharpen and the spectral window is reduced (Figure S6).[48] At the low-temperature limit of the solvent (178 K), the calculated $\chi_m T$ value is 0.163 cm^3 mol^{-1} K, corresponding to ca. 25% of a triplet species. These temperature-dependent changes in solution susceptibility are reversible and can be correlated with the changes in the 18 000 cm^{-1} band intensity with temperature (Figure 9). We were unable to expand the temperature range of our investigations due to the instability of [Cu**Sal**]$^+SbF_6^-$ in solvents other than CH_2Cl_2.

3. Discussion

Salen ligands are important systems for catalytic applications, and the modularity of the ligand structure, as well as the ability to form stable complexes with many metals in a variety of oxidation states, has accelerated their development. The electronic structure of oxidized metal–salen complexes is complicated by the potential ligand non-innocence. Numerous studies have focused on determining the factors that control the locus of oxidation in these compounds.[6,15,17–20,61] Ligand-based oxidation of Cu–salen complexes, to form coordinated phenoxyl radical species, has relevance to the oxidized form of galactose oxidase ($GOase_{ox}$), which contains a tyrosine radical ligand bound to a Cu(II) center.[2] We previously investigated Cu**Sal** and Cu**Sal**$^{\mathbf{red}}$ (Scheme 2) as small-molecule GOase models,[3,4] and found that minor changes to the ligand structure resulted in mechanistically distinct reactivity for the one-electron oxidized forms [Cu**Sal**]$^+$ and [Cu**Sal**$^{\mathbf{red}}$]$^+$. We now have investigated extensively the geometric and electronic structure of [Cu**Sal**]$^+$ and [Cu**Sal**$^{\mathbf{red}}$]$^+$ to gain insight into this differential reactivity as well as the nature of the localization/delocalization of the oxidation locus in these Cu–bis-phenoxide complexes.

The crystal structure of [Cu**Sal**]$^+$ (Figure 1) shows clearly a coordination sphere contraction upon one-electron oxidation of Cu**Sal**. In addition, the structure is more rigorously square-planar, indicative of a metal-based oxidation process and formation of a Cu(III) center. The ca. 0.04 Å reduction in Cu–ligand bond lengths (Table 2) is less than the reported contraction for other Cu complexes structurally characterized in both Cu(II) and Cu(III) oxidation states (0.1–0.17 Å)[24,26,62] and could be due to the limited flexibility of the **Sal** ligand toward coordination sphere contraction. Our previous work with the analogous [Ni**Sal**]$^+$ derivative also showed a coordination sphere contraction upon oxidation, even though this compound was established firmly to be a ligand-radical species in the solid state by spectroscopy;[18] ECDA calculations suggest that this contraction is due to a small increase in both L→M and M→L donation in the oxidized form (Table 3). In contrast, ECDA calculations for [Cu(III)**Sal**]$^+$ show that L→M donation is increased greatly in comparison to that in Cu**Sal**, highlighting the differences in bonding associated with metal-based as opposed to ligand-based oxidation in these systems. X-ray absorption spectroscopy in the solid state also supports a change in oxidation state from Cu(II) for Cu**Sal** to Cu(III) for [Cu**Sal**]$^+$. The change in the energy of the pre-edge feature from 8979.2 eV for Cu**Sal** to 8980.2 eV for [Cu**Sal**]$^+$ (Table 4) is consistent with a metal-centered oxidation process from Cu(II) to Cu(III).[33] This ca. 1 eV shift to higher energy for the Cu pre-edge transition matches the magnitude of the shift in the XPS Cu $2p_{3/2}$ and Cu $2p_{1/2}$ binding energies upon one-electron oxidation of Cu**Sal**.

The shift in the locus of oxidation from the ligand for [Ni**Sal**]$^+$ to the metal for [Cu**Sal**]$^+$ matches the trend for the monoanionic Ni and Cu dithiolenes.[12,63] In the case of Ni, the salen filled valence orbitals are higher in energy as compared to the d-orbital manifold, resulting in ligand non-innocence upon oxidation. For Cu, the Cu(II) d^9 configuration of Cu**Sal** results in the occupation of a higher energy, metal-centered ($d_{x^2-y^2}$-based) orbital, leading to a metal-centered oxidation process to [Cu**Sal**]$^+$. At the solid-state geometry of [Cu**Sal**]$^+$, the calculated singlet energy is predicted to be ca. 10 kcal mol^{-1} lower than the triplet energy. This large energy difference is consistent with solid-state magnetic measurements for [Cu**Sal**]$^+SbF_6^-$ showing that the compound is diamagnetic ($S = 0$ ground state), with no evidence for population of a higher energy triplet state at 300 K.

Interestingly, VT studies of [Cu**Sal**]$^+$ by absorption and ^{1}H NMR spectroscopy show that [Cu**Sal**]$^+$ exists in a spin equilibrium in solution that is reversible with temperature. The ^{1}H NMR spectrum at 295 K (Figure S6) indicates that a substantial amount of a paramagnetic species is present, which is attributed to the presence of a ferromagnetically coupled Cu(II)–ligand-radical species, [Cu(II)**Sal**$^\bullet$]$^+$. Based on the solid-state structure of [Cu**Sal**]$^+SbF_6^-$, and

the anticipated minor structural changes in solution, the magnetic orbitals of the Cu(II) ion ($d_{x^2-y^2}$) and of the phenoxyl radical (π-orbital) are orthogonal.[64] A spin density plot (Figure S7)[48] of the DFT geometry-optimized triplet species displays the unpaired electrons in these orbitals. The temperature dependence of the magnetic susceptibility for [Cu**Sal**]$^+SbF_6^-$ in a CH_2Cl_2 solution is rationalized in terms of an equilibrium between a diamagnetic Cu(III) species and a paramagnetic, ferromagnetically coupled Cu(II) complex, in which the more strongly bonded species, Cu(III), is favored at low temperature (Scheme 3). We were unable to probe directly this equilibrium by EPR, as the oxidation of Cu**Sal** in solution leads to an EPR-silent species (<5% of original intensity, 300 to 4 K).[3,65] This signal loss upon oxidation can be rationalized by the presence of a low-spin, diamagnetic Cu(III) d^8 species or a ferromagnetically coupled Cu(II)–ligand-radical species ($S = 1$) with a large zero-field splitting.[66] The fact that the spin equilibrium favors the Cu(III) species at lower temperatures decreases further the likelihood of detecting a triplet EPR signal.

The spin equilibrium is evident in the VT UV–vis data for [Cu**Sal**]$^+$ (Figure 6). Upon cooling from 298 to 190 K, the 18 000 cm^{-1} band approximately doubles in intensity and shifts to slightly higher energy (ca. 150 cm^{-1}), correlating with the change in the solution magnetic susceptibility. The increased intensity of this LMCT band, coupled with the shift of the λ_{max} to higher energy, is consistent with greater metal–ligand covalency; TD-DFT calculations (Table 6) predict the visible band to be higher in energy and of greater intensity for the singlet calculation in comparison to the triplet calculation. The calculated electronic energies for the geometry optimized triplet ([Cu(II)**Sal**$^\bullet$]$^+$) and singlet ([Cu(III)**Sal**]$^+$) states in a CH_2Cl_2 polarized continuum model (PCM) solvent model[67] incorrectly predict the triplet species to be lower in energy by 2.5 kcal mol^{-1} at 300 K. The calculated free energy difference is 1.8 kcal mol^{-1} at 200 K, and 0.7 kcal mol^{-1} at 0 K, supporting the nearly isoenergetic nature of these two electronic descriptions. Solid-state susceptibility measurements of [Cu**Sal**]$^+SbF_6^-$ show that this spin equilibrium is not operative in the solid state. In addition, VT solid-state mull UV–vis–NIR spectra of a powdered crystalline sample of [Cu**Sal**]$^+$ do not show any large intensity changes in the temperature range 295 to 5 K (Figure S8).[48]

Variable-temperature absorption studies and susceptibility studies via the Evans method (Figure S9)[48] of the tetrahydro-salen derivative [Cu**Sal^{red}**]$^+$ in solution do not exhibit significant changes. Solution susceptibility measurements support that the triplet Cu(II)–ligand-radical species ([Cu(II)**Sal$^{red\,\bullet}$**]$^+$; $\mu_{eff} = 2.5\,\mu_B$ at 295 K) is stabilized in the temperature range studied (295 to 180 K).[68] These results indicate that the more geometrically flexible and electron-rich tetrahydrosalen ligand stabilizes the Cu(II)–ligand-radical form and show how subtle changes to the electronic properties of the ligand can affect the electronic structure of the corresponding Cu complex. Characteristic phenoxyl bands are present in the rR spectrum of [Cu**Sal^{red}**]$^+$ (Figure 8) at 213 K with 413 nm excitation, providing further evidence of the stability of the ligand-radical form for this derivative. We were unable to detect the Cu(II)–phenoxyl-radical species for [Cu**Sal**]$^+$ by rR spectroscopy at either 213 K or 295 K. This result could be due to a shift of the phenoxyl bands to higher energy (413 nm is not sufficient for rR excitation[19]) or the fact that the spin equilibrium greatly reduces the intensity of the phenoxyl bands.

Comparison of a series of isostructural square-planar Cu–bis-phenoxide complexes (Scheme 4) permits a better description of the factors that influence the oxidation locus. For [Cu**L$_{amido}$**]$^-$, the powerful σ-donating ability of this tetranionic ligand stabilizes the Cu(III) oxidation state due to strong destabilization of the $d_{x^2-y^2}$ Cu orbital.[27] Replacing the amido donors with imines in [Cu**Sal**]$^+$ leads to lesser σ-donation and energy matching of the redox-active orbitals on the ligand and the metal center. The results presented here for [Cu**Sal**]$^+$ indicate that the geometric and electronic characteristics of the non-innocent **Sal** ligand framework are sufficient to stabilize both Cu(II) and Cu(III) oxidation states near room

temperature. However, the more geometrically flexible and electron-rich tetrahydrosalen derivative (**Sal^{red}**) affords the Cu(II)–ligand-radical form. These results contrast with a related series of oxidized Ni–N_2O_2 complexes, in which the locus of oxidation is exclusively ligand-based in all cases.[20]

The shift in the equilibrium from a ligand-radical species, [Cu(II)**Sal**$^{\bullet}$]$^+$, to a high-valent metal species, [Cu(III)**Sal**]$^+$, at low temperature is similar to the temperature-dependent valence tautomerism observed in numerous metal–dioxolene complexes.[10,69,70] Both the redox-active orbitals on the ligand and the metal need to be of similar energies to allow for reversible electron transfer to occur. Thermodynamic parameters for the equilibrium ([Cu(III)**Sal**]$^+$ ⇄ [Cu(II)**Sal**$^{\bullet}$]$^+$) were obtained by fitting the VT solution susceptibility data ($\Delta H° = 0.56 \pm 0.01$ kcal mol^{-1}, $\Delta S° = 2.0 \pm 0.1$ cal K^{-1} mol^{-1}; Figure 9) and suggest that the ligand-radical high-spin metal form is entropically stabilized, similar to the dioxolene systems,[71] while the high-valent metal species is enthalpically stabilized. Our computational results show that the coordination sphere bond lengths are shorter for d^8 [Cu(III)**Sal**]$^+$ as compared with the triplet species d^9 [Cu(II)**Sal**$^{\bullet}$]$^+$ (Table 2) and, in combination with the experimental analysis of [Cu**Sal**]$^+$ in solution, suggest that the observed equilibrium favors the Cu(III) species at lower temperature. The small magnitude of the thermodynamic parameters for [Cu**Sal**]$^+$ in comparison to those reported for many metal–dioxolene systems[10] is consistent with the relatively minor predicted change in bond lengths accompanying the shift in the locus of oxidation for [Cu**Sal**]$^+$. While temperature-dependent valence tautomerism between Cu(II)–catecholate and Cu(I)–semiquinonate species has been reported,[70,72] this is the first account of a spin equilibrium involving a Cu–phenoxide complex. Interestingly, in the case of [Ni**Sal**]$^+$, the shift in the locus of oxidation from the ligand to the metal is due to large changes in the ligand field associated with axial ligation at low temperature.[18] The binding of exogenous ligands to square-planar Ni(II)–semiquinone and Ni(III)–catecholate complexes has also been reported to lead to metal spin-state changes and/or valence tautomerism.[73] Axial ligation presumably does not have a significant role in the equilibrium for [Cu**Sal**]$^+$ under the conditions used here, as axial coordination would bias the equilibrium in favor of the d^9 [Cu(II)**Sal**$^{\bullet}$]$^+$ form at low temperature. Indeed, the small but positive entropy value measured for the equilibrium ([Cu(III)-**Sal**]$^+$ ⇄ [Cu(II)**Sal**$^{\bullet}$]$^+$) indicates that the formation of d^9 [Cu(II)**Sal**$^{\bullet}$]$^+$ at higher temperatures is not associated with axial ligand binding.[74] The [Cu**Sal**]$^+$ spin equilibrium presumably occurs without a change in coordination number, and thus the ligand-field changes associated with the shift in the locus of oxidation are more subtle in comparison to those in the Ni systems.[75] The similarity in energy between the [Cu(II)**Sal**$^{\bullet}$]$^+$ and [Cu(III)**Sal**]$^+$ forms can be compared to the well-studied isomeric μ-η^2: η^2-peroxodicopper(II) (**^{S}P**) and bis(μ-oxo)dicop-per(III) (**O**) complexes with aliphatic and/or aromatic amine ligands.[76] The similar square-planar geometrical preference of the Cu(II) d^9 and Cu(III) d^8 oxidation states, coupled with the flexibility of the $[Cu_2O_2]^{2+}$ core toward contraction and expansion, results in the **^{S}P** and **O** forms being of similar energy.

4. Summary

We have shown in this work that the locus of oxidation in the Cu–salen derivative [Cu**Sal**]$^+$ is metal-based, resulting in a Cu(III) species in the solid state. Surprisingly, the dianionic square-planar salen ligand is able to stabilize the Cu(III) oxidation state. In solution, a temperature-dependent equilibrium is proposed to exist between high-valent metal ([Cu(III)**Sal**]$^+$) and ligand-radical ([Cu(II)**Sal**$^{\bullet}$]$^+$) forms, indicating nearly isoenergetic species. This is the first account of a temperature-dependent spin equilibrium for a Cu complex outside of the well-studied dioxolene systems. Variable-temperature solution susceptibility and absorption spectroscopy show that the diamagnetic [Cu(III)**Sal**]$^+$ species is stabilized at low temperature; however, the increased flexibility of the complex toward coordination sphere contraction and expansion in solution presumably allows for stabilization of the two forms in this medium.

Preliminary work with the oxidized tetrahydrosalen derivative [Cu**Sal**$^{\mathbf{red}}$]$^+$ suggests that this species exists as a temperature-invariant Cu(II)–ligand-radical species in solution and shows how subtle changes to the electronic properties of the ligand can affect the electronic structure of the Cu complex.

Evaluation of the electronic structure of [Cu**Sal**]$^+$ and [Cu**Sal**$^{\mathbf{red}}$]$^+$ allows us to speculate on the origin of the different reactivities of these compounds with benzyl alcohol. The slower reactivity of [Cu**Sal**]$^+$ as compared with [Cu**Sal**$^{\mathbf{red}}$]$^+$,[4] even though [Cu**Sal**]$^+$ is a much stronger oxidant, could be due to the presence of the [Cu(III)**Sal**]$^+$ species in solution. The Cu(III) d^8 species [Cu(III)**Sal**]$^+$ disfavors axial substrate binding to a greater extent than the Cu(II) d^9 derivative [Cu(II)**Sal**$^{\mathbf{red}}$]$^+$. Substrate binding allows the thermodynamically weaker oxidant to react more rapidly via substrate preorganization, the same means by which enzymes such as GOase are capable of performing highly selective transformations under mild conditions. We are currently probing how subtle changes to ligand electronics influence the locus of oxidation in other Cu–bis-phenoxide derivatives, and the reactivity of those derivatives with externally added substrates.

5. Experimental Section

5.1. Materials and Methods

All solvents and reagents were obtained from commercial sources and used as received unless noted otherwise. Cu**Sal**,[77] Cu**Sal**$^{\mathbf{red}}$ and [Cu**Sal**$^{\mathbf{red}}$]$^+$,[3] and [PPh_4][Cu-*N*, *N*′-*o*-phenylene-bis (methylamide)][26] were prepared as reported previously. Data collection and structure solution for the crystal structure of [Cu**Sal**]$^+SbF_6^-$ were conducted at the X-ray Crystallographic Laboratory, S146 Kolthoff Hall, Department of Chemistry, University of Minnesota. Details are available in the CIF file (Supporting Information). Cyclic voltammetry was performed using a BAS CV-40 potentiometer, a Ag wire reference electrode, a platinum disk working electrode, and a Pt wire counter electrode with 0.1 M Bu_4NClO_4 solutions in CH_2Cl_2. Ferrocene was used as an internal standard. X-band EPR spectra were collected with a Bruker EMX spectrometer using an ER041XG microwave bridge and an ER4102ST cavity for experiments conducted at 298 to 77 K. From 77 to 4 K, an Oxford ITC503 temperature controller with an EPR 900 continuous flow cryostat were used. UV–vis–NIR spectroscopy was performed using a Cary 500 dual-beam spectrophotometer. Variable-temperature UV–vis spectroscopy was performed using a Cary 50 spectrophotometer with a custom-designed immersable fiber-optic quartz probe with variable path length (1 and 10 mm; Hellma, Inc.). Constant temperatures were maintained by either a cooling bath (Kinetic Systems, New York) or a dry ice/acetone bath. Solution temperatures were directly monitored by insertion of an Omega temperature probe in the solutions. Variable-temperature Evans method ^1H NMR measurements were performed on a Varian Inova 300 MHz instrument in CD_2Cl_2, and diamagnetic corrections were estimated using Pascal's constants. Solvent contraction was accounted for in all variable-temperature studies. Analytical services were provided by Desert Analytics (Tucson, AZ). X-ray photoelectron spectra were recorded on a Thermo VG Scientific Model Theta Probe spectrometer using Al Kα radiation (1486.6 eV) operating at 15 kV and 3 mA. The solid sample was dispersed on an In film, and the carbon 1s binding energy (284.5 eV) was used to calibrate the binding energy.

5.2. Synthesis

Cu**Sal** (0.103 g, 0.17 mmol) and $AgSbF_6$ (0.058 g, 0.17 mmol) were placed in a scintillation vial under an inert atmosphere, and CH_2Cl_2 (5 mL) was added. A purple suspension formed immediately. The suspension was stirred for 1 h and filtered through a Celite pad, and the solvent was removed *in vacuo*. The purple solid was dissolved in a minimum of CH_2Cl_2 (1 mL), and pentane (10 mL) was added to precipitate the material. The solid was isolated, washed

with pentane, and dried under vacuum to afford [Cu**Sal**]$^{+}SbF_6^{-}$ as a purple solid (0.117 g, 82% yield). Elemental analysis calculated for $C_{36}H_{52}N_2O_2CuSbF_6$: C, 51.23; H, 6.21; N, 3.32. Found: C, 51.02; H, 6.28; N, 3.24. Crystals suitable for X-ray analysis were grown via pentane diffusion into a concentrated CH_2Cl_2 solution of [Cu**Sal**]$^{+}SbF_6^{-}$.

5.3. Solid-State Magnetic Susceptibility

Solid-state variable-temperature magnetic susceptibility data were collected on a Quantum Design MPMS-XL super conducting quantum interference device. Powdered microcrystalline samples of Cu**Sal** or [Cu**Sal**]$^{+}SbF_6^{-}$ were added to a gel capsule and held in place with eicosane (Aldrich). Data were collected in the temperature range 5–300 K at 5000 Oe and corrected for the diamagnetic signal of the gel capsule and eicosane. Diamagnetic corrections for the sample were estimated using Pascal's constants. The data for Cu**Sal** were fit to a Curie–Weiss law (C = 0.405, θ= −0.554 K). The data for [Cu**Sal**]$^{+}SbF_6^{-}$ were fit with a 4% paramagnetic impurity of Cu**Sal** (estimated from the low-temperature data) and were essentially diamagnetic in the temperature range studied (Figure S1).[48]

5.4. Resonance Raman Spectroscopy

Resonance Raman spectra were obtained on a SpectraPro-300i spectrometer (Acton Research) with a 2400-groove grating, a Beamlok 2060 Kr ion laser (Spectra-Physics), a holographic supernoch filter (Kaiser Optical Systems), and an LN-1100PB CCD detector (Princeton Instruments) cooled with liquid N_2. Spectra were collected on solvated samples (1 mM) in spinning cells (2 cm diameter, 1500 rpm) at variable temperatures (293 to 213 K) at an excitation wavelength λ_{ex} = 413.1 nm (20 mW), 90° scattering geometry, and 5 min data accumulation. Peak frequencies were calibrated relative to indene and CCl_4 standards (accurate to ±1 cm^{-1}). During each Raman experiment, UV–vis spectra were collected simultaneously on a PMA-11 CCD spectrophotometer (Hamamatsu) with a Photal MC-2530 (D_2/W_2) light source (Otsuka Electronic Co.).

5.5. X-ray Absorption Spectroscopy

Cu K-edge and L-edge XAS data were collected at the Stanford Synchrotron Radiation Laboratory under dedicated ring conditions of 60–100 mA and 3 GeV.

5.5.1. Cu K-Edge—Cu K-edge data were recorded on the wiggler beam line 7–3. A Si (220) monochromator was used for energy selection and detuned (50%) to minimize higher harmonic components of the X-ray beam. The samples were finely ground with boron nitride and pressed into a 1 mm aluminum spacer. The spacer was sealed with 37 μm Kapton windows and inserted into an aluminum XAS powder sample cell. The sample cell was precooled in liquid N_2 before insertion into an Oxford Instruments CF1208 continuous flow liquid helium cryostat, in which the samples were maintained at 10–15 K during data collection. Data were measured in transmission mode with N_2-filled ionization chambers before and after the sample. Internal energy calibration was performed by simultaneous measurement of the transmission signal through a Cu reference foil. The first inflection point of the copper reference data was aligned to 8980.3 eV. Data of four scans were averaged and were processed by fitting a smooth polynomial to the pre-edge region, which was background-subtracted from the entire spectrum. A three-region cubic spline was used to model the smooth background above the edge. Data were normalized by subtracting the spline and normalizing the post-edge data to 1.0. EXAFS data were fit with the EXAFSPAK[78] program, using theoretical phase and amplitude parameters derived from FeFF7.0.[79] Absorber–scatterer distances (R, Å) and Debye–Waller factors (σ^2, Å^2) were varied independently for each component in each fit. Additionally, the E_0 (eV) value, or the energy onset of photoionization, was also varied for each fit but kept to

a common value for all components of a given fit, and coordination numbers were kept constant. Further fitting information is available in Table S1.[48]

The intensities and energies of the 1s→3d pre-edge transitions for each complex were quantified by simultaneously fitting pseudo-Voigt line shapes to the data and the second derivative of the data using the EDG_FIT program. The energy position, half-width, and amplitude of each feature were allowed to vary within each fit. A background pseudo-Voigt function was used to model the rising absorption edge shape. The entire fit was performed over four energyranges(8976–8983,8976–8984,8976–8985, and 8976–8986 eV) to ensure that the background chosen did not affect the quantitative fit. The approximate peak area was measured as the product of the peak amplitude and the full width at half-maximum of the pre-edge feature. The stated peak areas are the averages of the areas over the four energy ranges used, and standard deviations were calculated to estimate the variability of the fits.

5.5.2. Cu L-Edge—Cu L-edge data were recorded on the 31 pole wiggler beam line 10-1. The radiation was monochromatized using a spherical grating monochromator at the 1000 lines mm^{-1} setting using 20 μm entrance and exit slits to define the beam. Solid samples were finely ground and applied across double-sided adhesive conductive graphite tape affixed to an aluminum support aligned at 45° to the incident beam. The vacuum chamber was maintained at a pressure of 10^{-5} Torr or lower and isolated from the UHV beam line by a 1000 Å diamond window. Sample measurement was performed in total electron yield mode using a Channeltron electron multiplier (I_1) aligned at 45° to the sample and 90° to the incident beam (I_0). The photocurrent of a gold grid reference monitor was used to flux-normalize (I_1/I_0) the sample signal. Data were linearly calibrated using CuF_2 as a two-point reference sample prior to and subsequent to each sample measurement, aligning the L_3 edge of CuF_2 with 930.5 eV and the L_2 edge with 950.5 eV. In all cases, the maximum calibration shift was ≤0.1 eV. For each sample, multiple scans were collected. The Cu**Sal** sample showed no indication of photoreduction; however, significant photoreduction of [Cu**Sal**]$^+$ and [PPh_4][Cu-*N*, *N*′-*o*-phenylene-bis(methylamide)][26] was observed during data collection.

5.6. Calculations

Geometry optimizations were performed using the Gaussian 03 program,[80] the B3LYP functional,[40] and the 6–31G(d) basis set on all atoms, as this double-ζ optimization gave the best agreement with the solid-state structural data. Broken symmetry optimizations for [Cu**Sal**]$^+$ from all starting geometries collapsed to a singlet solution in all cases, suggesting that the [Cu(III)**Sal**]$^+$ state is electronically lower in energy than the antiferromagnetically coupled [Cu(II)**Sal**$^\bullet$]$^+$ state. The free energies of the singlet and triplet states for [Cu**Sal**]$^+$ were computed from the gas-phase optimized structures as a sum of electronic energy, thermal corrections to free energy, and free energy of solvation. Single-point calculations for energetic analysis were performed using the BLYP[81] functional and the TZVP basis set of Ahlrichs[82] on all atoms with a PCM for CH_2Cl_2 (dielectric $\varepsilon = 8.94$).[67] AOMIX[42–44] was used for ECDA, as well as for determining atomic orbital compositions using Mulliken Population Analysis and Mayer[41] bond orders. The intensities of the 30 lowest-energy electronic transitions were calculated by TD-DFT[54] with the BLYP functional and TZVP basis set on all atoms. A complete list of the calculated transitions is available.[48]

Acknowledgements

This work was supported by NIH grant GM-50730 (TDPS), start-up funding from the CSUC College of Natural Sciences (E.C.W.), and an NSERC postdoctoral scholarship (T.S.). We acknowledge Prof. Yoshinori Naruta and Prof. Fumito Tani of Kyushu University for measurement of the resonance Raman spectra. Stanford Synchrotron Radiation Laboratory operations are funded by the U.S. Department of Energy, Office of Basic Energy Services. We thank Prof. E. I. Solomon and the Solomon group for use of the EPR and UV–vis–NIR instruments, and Dr. S. Gorelsky for helpful DFT discussions. Eric Samulon and Prof. Ian Fisher at Stanford are acknowledged for the use of the SQUID

magnetometer. Benjamin E. Kucera and Victor G. Young, Jr., at the University of Minnesota X-Ray Crystallographic Laboratory are thanked for X-ray analysis.

References

1. Stubbe J, van der Donk WA. Chem Rev 1998;98:705. [PubMed: 11848913]
2. Whittaker JW. Chem Rev 2003;103:2347. [PubMed: 12797833]
3. Pratt RC, Stack TDP. J Am Chem Soc 2003;125:8716. [PubMed: 12862453]
4. Pratt RC, Stack TDP. Inorg Chem 2005;44:2367. [PubMed: 15792472]
5. (a) Wang YD, DuBois JL, Hedman B, Hodgson KO, Stack TDP. Science 1998;279:537. [PubMed: 9438841] (b) Shimazaki Y, Huth S, Hirota S, Yamauchi O. Inorg Chim Acta 2002;331:168. (c) Shimazaki Y, Huth S, Odani A, Yamauchi O. Angew Chem, Int Ed 2000;39:1666. (d) Thomas F. Eur J Inorg Chem 2007:2379. (e) Thomas F, Gellon G, Gautier-Luneau I, Saint-Aman E, Pierre JL. Angew Chem, Int Ed 2002;41:3047. (f) Halfen JA, Jazdzewski BA, Mahapatra S, Berreau LM, Wilkinson EC, Que L Jr, Tolman WB. J Am Chem Soc 1997;119:8217. (g) Michel F, Thomas F, Hamman S, Philouze C, Saint-Aman E, Pierre JL. Eur J Inorg Chem 2006:3684. (h) Zurita D, Ménage S, Pierre JL, Saintaman E. New J Chem 1997;21:1001. (i) Chaudhuri P, Hess M, Florke U, Wieghardt K. Angew Chem, Int Ed 1998;37:2217. (j) Chaudhuri P, Hess M, Müller J, Hildenbrand K, Bill E, Weyhermüller T, Wieghardt K. J Am Chem Soc 1999;121:9599. (k) Itoh S, Taki M, Takayama S, Nagatomo S, Kitagawa T, Sakurada N, Arakawa R, Fukuzumi S. Angew Chem, Int Ed 1999;38:2774. (l) Saint-Aman E, Ménage S, Pierre JL, Defrancq E, Gellon G. New J Chem 1998;22:393. (m) Taki M, Hattori H, Osako T, Nagatomo S, Shiro M, Kitagawa T, Itoh S. Inorg Chim Acta 2004;357:3369. (n) Taki M, Kumei H, Itoh S, Fukuzumi S. J Inorg Biochem 2000;78:1. [PubMed: 10714699] (o) Vaidyanathan M, Palaniandavar M, Gopalan RS. Ind J Chem A 2003;42:2210. (p) Zueva E, Walton PH, McGrady JE. Dalton Trans 2006:159.
6. Thomas F, Jarjayes O, Duboc C, Philouze C, Saint-Aman E, Pierre JL. Dalton Trans 2004:2662. [PubMed: 15514749]
7. Sokolowski A, Leutbecher H, Weyhermuller T, Schnepf R, Both E, Bill E, Hildebrandt P, Wieghardt K. J Biol Inorg Chem 1997;2:444.
8. Benisvy L, Blake AJ, Collison D, Davies ES, Garner CD, McInnes EJL, McMaster J, Whittaker G, Wilson C. Chem Commun 2001:1824.
9. Jorgensen CK. Coord Chem Rev 1966;1:164.
10. Pierpont CG. Coord Chem Rev 2001;216:99.
11. Chaudhuri P, Wieghardt K. Prog Inorg Chem 2001;50:151.
12. Ray K, Petrenko T, Wieghardt K, Neese F. Dalton Trans 2007:1552.
13. (a) Darensbourg DJ. Chem Rev 2007;107:2388. [PubMed: 17447821] (b) McGarrigle EM, Gilheany DG. Chem Rev 2005;105:1563. [PubMed: 15884784] (c) Irie R, Noda K, Ito Y, Matsumoto N, Katsuki T. Tetrahedron Lett 1990;31:7345. (d) Jacobsen EN, Zhang W, Muci AR, Ecker JR, Deng L. J Am Chem Soc 1991;113:7063. (e) Canali L, Sherrington DC. Chem Soc Rev 1999;28:85.
14. (a) Audebert P, Capdevielle P, Maumy M. New J Chem 1991;15:235. (b) Pasini A, Bernini E, Scaglia M, DeSantis G. Polyhedron 1996;15:4461. (c) Abuelwafa SM, Issa RM, McAuliffe CA. Inorg Chim Acta 1985;99:103. (d) Böttcher A, Elias H, Jäger EG, Langfelderova H, Mazur M, Müller L, Paulus H, Pelikan P, Rudolph M, Valko M. Inorg Chem 1993;32:4131. (e) Freire C, de Castro B. J Chem Soc, Dalton Trans 1998:1491.
15. (a) Benisvy L, Kannappan R, Song YF, Milikisyants S, Huber M, Mutikainen I, Turpeinen U, Garnez P, Bernasconi L, Baerends EJ, Hartl F, Reedijk J. Eur J Inorg Chem 2007:631. (b) Kurahashi T, Kobayashi Y, Nagatomo S, Tosha T, Kitagawa T, Fujii H. Inorg Chem 2005;44:8156. [PubMed: 16241166] (c) Bryliakov KP, Talsi EP. Angew Chem, Int Ed 2004;43:5228. (d) Bryliakov KP, Talsi EP. Chem Eur J 2007;13:8045.
16. Shimazaki Y, Tani F, Fukui K, Naruta Y, Yamauchi O. J Am Chem Soc 2003;125:10512. [PubMed: 12940721]
17. Shimazaki Y, Yajima T, Tani F, Karasawa S, Fukui K, Naruta Y, Yamauchi O. J Am Chem Soc 2007;129:2559. [PubMed: 17290991]
18. Storr T, Wasinger EC, Pratt RC, Stack TDP. Angew Chem, Int Ed 2007;46:5198.

19. Kurahashi T, Kikuchi A, Tosha T, Shiro Y, Kitagawa T, Fuji H. Inorg Chem 2008;47:1674. [PubMed: 18237118]

20. (a) Rotthaus O, Jarjayes O, Thomas F, Philouze C, Del Valle CP, Saint-Aman E, Pierre JL. Chem Eur J 2006;12:2293. (b) Rotthaus O, Thomas F, Jarjayes O, Philouze C, Saint-Aman E, Pierre JL. Chem Eur J 2006;12:6953.

21. (a) Snodin MD, Ould-Moussa L, Wallmann U, Lecomte S, Bachler V, Bill E, Hummel H, Weyhermüller T, Hildebrandt P, Wieghardt K. Chem Eur J 1999;5:2554. (b) Muller J, Kikuchi A, Bill E, Weyhermuller T, Hildebrandt P, Ould-Moussa L, Wieghardt K. Inorg Chim Acta 2000;297:265. (c) Chaudhuri P, Verani CN, Bill E, Bothe E, Weyhermuller T, Wieghardt K. J Am Chem Soc 2001;123:2213. [PubMed: 11456867] (d) Herebian D, Bothe E, Neese F, Weyhermueller T, Weighardt K. J Am Chem Soc 2003;125:9116. [PubMed: 15369369] (e) Blanchard S, Neese F, Bothe E, Bill E, Weyhermuller T, Wieghardt K. Inorg Chem 2005;44:3636. [PubMed: 15877448] (f) Chlopek K, Bothe E, Neese F, Weyhermuller T, Wieghardt K. Inorg Chem 2006;45:6298. [PubMed: 16878939] (g) Lu CC, Bill E, Weyhermuller T, Bothe E, Wieghardt K. J Am Chem Soc 2008;130:3181. [PubMed: 18284242]

22. (a) Blackmore KJ, Lal N, Ziller JW, Heyduk AF. J Am Chem Soc 2008;130:2728. [PubMed: 18266370] (b) Buttner T, Geier J, Frison G, Harmer J, Calle C, Schweiger A, Schonberg H, Grutzmacher H. Science 2005;307:235. [PubMed: 15653498] (c) Haneline MR, Heyduk AF. J Am Chem Soc 2006;128:8410. [PubMed: 16802801] (d) Konigsmann M, Donati N, Stein D, Schonberg H, Harmer J, Sreekanth A, Grutzmacher H. Angew Chem, Int Ed 2007;46:3567. (e) Maire P, Konigsmann M, Sreekanth A, Harmer J, Schweiger A, Grutzmacher H. J Am Chem Soc 2006;128:6578. [PubMed: 16704256] (f) Miyazato Y, Wada T, Tanaka K. Bull Chem Soc Jpn 2006;79:745. (g) Ringenberg MR, Kokatam SL, Heiden ZM, Rauchfuss TB. J Am Chem Soc 2008;130:788. [PubMed: 18163627]

23. Melnik M, Kabesova M. J Coord Chem 2000;50:323.

24. Diaddario LL, Robinson WR, Margerum DW. Inorg Chem 1983;22:1021.

25. Hanss J, Kruger HJ. Angew Chem, Int Ed 1996;35:2827.

26. Ruiz R, Surville-Barland C, Aukauloo A, Anxolabehere-Mallart E, Journaux Y, Cano J, Muñoz MC. J Chem Soc, Dalton Trans 1997:745.

27. Anson FC, Collins TJ, Richmond TG, Santarsiero BD, Toth JE, Treco B. J Am Chem Soc 1987;109:2974.

28. Cervera B, Sanz JL, Ibáñez MJ, Vila GL, Loret F, Julve M, Ruiz R, Ottenwaelder X, Aukauloo A, Poussereau S, Journaux Y, Muñoz MC. J Chem Soc, Dalton Trans 1998:781.

29. Speier G, Fulop V. J Chem Soc, Chem Commun 1990:905.

30. Maeda H, Ishikawa Y, Matsuda T, Osuka A, Furuta H. J Am Chem Soc 2003;125:11822. [PubMed: 14505396]

31. (a) Santo R, Miyamoto R, Tanaka R, Nishioka T, Sato K, Toyota K, Obata M, Yano S, Kinoshita I, Ichimura A, Takui T. Angew Chem, Int Ed 2006;45:7611. (b) Krebs C, Glaser T, Bill E, Weyhermuller T, Meyer-Klaucke W, Wieghardt K. Angew Chem, Int Ed 1999;38:359.

32. (a) DuBois JL, Mukherjee P, Collier AM, Mayer JM, Solomon EI, Hedman B, Stack TDP, Hodgson KO. J Am Chem Soc 1997;119:8578. (b) Root DE, Henson MJ, Machonkin T, Mukherjee P, Stack TDP, Solomon EI. J Am Chem Soc 1998;120:4982. (c) Mahadevan V, DuBois JL, Hedman B, Hodgson KO, Stack TDP. J Am Chem Soc 1999;121:5583. (d) Henson MJ, Mukherjee P, Root DE, Stack TDP, Solomon EI. J Am Chem Soc 1999;121:10332. (e) Cole AP, Mahadevan V, Mirica LM, Ottenwaelder X, Stack TDP. Inorg Chem 2005;44:7345. [PubMed: 16212361] (f) Mahapatra S, Halfen J, Wilkinson E, Pan G, Cramer CJ, Que L Jr, Tolman WB. J Am Chem Soc 1995;117:8865. (g) Mahapatra S, Young VG, Kaderli S, Zuberbühler AD, Tolman WB. Angew Chem, Int Ed 1997;36:130. (h) Itoh S, Taki M, Nakao H, Holland PL, Tolman WB, Que L Jr, Fukuzumi S. Angew Chem, Int Ed 2000;39:398.

33. DuBois JL, Mukherjee P, Stack TDP, Hedman B, Solomon EI, Hodgson KO. J Am Chem Soc 2000;122:5775.

34. (a) Bertz SH, Cope S, Dorton D, Murphy M, Ogle CA. Angew Chem, Int Ed 2007;46:7082. (b) Bertz SH, Cope S, Murphy M, Ogle CA, Taylor BJ. J Am Chem Soc 2007;129:7208. [PubMed: 17506552] (c) Hu HP, Snyder JP. J Am Chem Soc 2007;129:7210. [PubMed: 17506553] (d) Ribas X, Jackson DA, Donnadieu B, Mahia J, Parella Xifra R, Hedman B, Hodgson KO, Llobet A, Stack TDP. Angew

Chem, Int Ed 2002;41:2991. (e) Huffman LM, Stahl SS. J Am Chem Soc 2008;130:9196. [PubMed: 18582057]

35. (a) Mirica LM, Vance M, Rudd DJ, Hedman B, Hodgson KO, Solomon EI, Stack TDP. Science 2005;308:1890. [PubMed: 15976297] (b) Company A, Palavicini S, Garcia-Bosch I, Mas-Balleste R, Que L, Rybak-Akimova EV, Casella L, Ribas X, Costas M. Chem Eur J 2008;14:3535.
36. Connelly NG, Geiger WE. Chem Rev 1996;96:877. [PubMed: 11848774]
37. Bunce S, Cross RJ, Farrugia LJ, Kunchandy S, Meason LL, Muir KW, O'Donnell M, Peacock RD, Stirling D, Teat SJ. Polyhedron 1998;17:4179.
38. (a) Benisvy L, Blake AJ, Collison D, Davies ES, Garner CD, McInnes EJL, McMaster J, Whittaker G, Wilson C. Dalton Trans 2003:1975. (b) Sokolowski A, Bothe E, Bill E, Weyher-müller T, Wieghardt K. Chem Commun 1996:1671.
39. Hanss J, Beckmann A, Kruger HJ. Eur J Inorg Chem 1999:163.
40. (a) Becke AD. J Chem Phys 1993;98:5648. (b) Stephens PJ, Devlin FJ, Chabalowski CF, Frisch MJ. J Phys Chem 1994;98:11623.
41. (a) Mayer I. Int J Quantum Chem 1986;29:477. (b) Mayer I. Int J Quantum Chem 1986;29:73.
42. Gorelsky, SI. AOMix: Program for Molecular Orbital Analysis. University of Ottawa; Ottawa, Canada: 2007. http://www.sg-chem.net/
43. Gorelsky SI, Lever ABP. J Organomet Chem 2001;635:187.
44. Gorelsky SI, Solomon EI. Theor Chem Acc 2008;119:57.
45. The net polarization of the ligand and the metal is ca. 5–10% of the net charge transfer in all ECDA analyses in these complexes, and thus the contribution of polarization of the L→Cu and Cu→L as quantified here is ignored.
46. Kau LS, Spira-Solomon DJ, Penner-Hahn JE, Hodgson KO, Solomon EI. J Am Chem Soc 1987;109:6433.
47. Westre TE, Kennepohl P, DeWitt JG, Hedman B, Hodgson KO, Solomon EI. J Am Chem Soc 1997;119:6297.
48. See Supporting Information.
49. EXAFS analysis typically cannot distinguish between atoms that differ in Z by 1 (e.g., O and N). Scott RA. Methods Enzymol 1985;117:414.
50. (a) de Groot F. Chem Rev 2001;101:1779. [PubMed: 11709999] (b) de Groot F. Coord Chem Rev 2005;249:31. (c) DeBeer George S, Metz M, Szilagyi RK, Wang H, Cramer SP, Lu Y, Tolman WB, Hedman B, Hodgson KO, Solomon EI. J Am Chem Soc 2001;123:5757. [PubMed: 11403610]
51. George SJ, Lowery MD, Solomon EI, Cramer SP. J Am Chem Soc 1993;115:2968.
52. George SD, Metz M, Szilagyi RK, Wang HX, Cramer SP, Lu Y, Tolman WB, Hedman B, Hodgson KO, Solomon EI. J Am Chem Soc 2001;123:5757. [PubMed: 11403610]
53. Sarangi R, Aboelella N, Fujisawa K, Tolman WB, Hedman B, Hodgson KO, Solomon EI. J Am Chem Soc 2006;128:8286. [PubMed: 16787093]
54. Casida, ME. Recent Advances in Density Functional Methods. Chong, DP., editor. World Scientific; Singapore: 1995. p. 155 (b) Stratmann RE, Scuseria GE, Frisch MJ. J Chem Phys 1998;109:8218.
55. Gorelsky, SI. SWizard program. University of Ottawa; Ottawa, Canada: 2008. http://www.sg-chem.net/
56. Chen P, Root DE, Campochiaro C, Fujisawa K, Solomon EI. J Am Chem Soc 2003;125:466. [PubMed: 12517160]
57. (a) Sokolowski A, Muller J, Weyhermuller T, Schnepf R, Hildebrandt P, Hildenbrand K, Bothe E, Wieghardt K. J Am Chem Soc 1997;119:8889. (b) Mukherjee A, McGlashen ML, Spiro TG. J Phys Chem 1995;99:4912.
58. McGlashen ML, Eads DD, Spiro TG, Whittaker JW. J Phys Chem 1995;99:4918.
59. Schnepf R, Sokolowski A, Muller J, Bachler V, Wieghardt K, Hildebrandt P. J Am Chem Soc 1998;120:2352.
60. Evans DF. J Chem Soc 1959:2003.
61. Shimazaki Y, Huth S, Karasawa S, Hirota S, Naruta Y, Yamauchi O. Inorg Chem 2004;43:7816. [PubMed: 15554647]

62. Hanss J, Krüger HJ. Angew Chem, Int Ed 1996;35:2827.
63. (a) Ray K, Weyhermuller T, Neese F, Wieghardt K. Inorg Chem 2005;44:5345. [PubMed: 16022533] (b) Sarangi R, George SD, Rudd DJ, Szilagyi RK, Ribas X, Rovira C, Almeida M, Hodgson KO, Hedman B, Solomon EI. J Am Chem Soc 2007;129:2316. [PubMed: 17269767]
64. Muller J, Weyhermuller T, Bill E, Hildebrandt P, Ould-Moussa L, Glaser T, Wieghardt K. Angew Chem, Int Ed 1998;37:616.
65. X-band EPR spectra of [Cu**Sal**]$^{+}$ and [Cu**Sal**$^{\mathbf{red}}$]$^{+}$ at 4 K do not exhibit any half-field signals that would be associated with a triplet species.
66. Large zero-field splitting results in EPR transitions outside of the energy range of X-band EPR. (a) Dei A, Gatteschi D, Pardi L, Barra AL, Brunel LC. Chem Phys Lett 1990;175:589. (b) Berreau LM, Mahapatra S, Halfen JA, Houser RP, Young VG, Tolman WB. Angew Chem, Int Ed 1999;38:207.
67. (a) Barone V, Cossi M, Tomasi J. J Comput Chem 1998;19:404. (b) Tomasi J, Mennucci B, Cances E. J Mol Struct 1999;464:211. (c) Barone V, Cossi M, Tomasi J. J Chem Phys 1997;107:3210. (d) Miertus S, Scrocco E, Tomasi J. Chem Phys 1981;55:117.
68. The energy of the Cu K pre-edge feature of [Cu**Sal**$^{\mathbf{red}}$]$^{+}$ (frozen DCM solution) is 8979.2 eV, suggesting that it is a Cu(II)–ligand-radical complex.
69. (a) Adams DM, Noodleman L, Hendrickson DN. Inorg Chem 1997;36:3966. (b) Hendrickson DN, Pierpont CG. Top Curr Chem 2004;234:63.
70. (a) Rall J, Wanner M, Albrecht M, Hornung FM, Kaim W. Chem Eur J 1999;5:2802. (b) Speier G, Tyeklár Z, Toth P, Speier E, Tisza S, Rockenbauer A, Whalen AM, Alkire N, Pierpont CG. Inorg Chem 2001;40:5653. [PubMed: 11599966]
71. Shultz, DA. Magnetism: Molecules to Materials II. Miller, JS.; Drillon, M., editors. Wiley-VCH; Weinheim: 2001. p. 281
72. Ye SF, Sarkar B, Niemeyer M, Kaim W. Eur J Inorg Chem 2005:4735.
73. (a) Ohtsu H, Tanaka K. Inorg Chem 2004;43:3024. [PubMed: 15106994] (b) Ohtsu H, Tanaka K. Chem Eur J 2005;11:3420.
74. Youngblood MP, Margerum DW. Inorg Chem 1980;19:3068.
75. Addition of exogenous ligands such as pyridine to solutions of [Cu**Sal**]$^{+}$ at 295 or 196 K, to probe the effect of axial ligation on the spin equilibrium, results in rapid decomposition of the sample.
76. Mirica LM, Ottenwaelder X, Stack TDP. Chem Rev 2004;104:1013. [PubMed: 14871148]
77. Leung WH, Chan EYY, Chow EKF, Williams ID, Peng SM. J Chem Soc, Dalton Trans 1996:1229.
78. Rehr JJ, Deleon JM, Zabinsky SI, Albers RC. J Am Chem Soc 1991;113:5135.
79. George, GN. EXAFSPAK & EDG_FIT. Stanford Synchrotron Radiation Laboratory, Stanford Linear Accelerator Center, Stanford University; Stanford, CA: 2000.
80. Frisch, MJT., et al. Gaussian 03, Revision C.02. Gaussian, Inc; Wallingford, CT: 2004.
81. (a) Becke AD. Phys Rev A 1988;38:3098. [PubMed: 9900728] (b) Lee CT, Yang WT, Parr RG. Phys Rev B 1988;37:785.
82. (a) Schafer A, Horn H, Ahlrichs R. J Chem Phys 1992;97:2571. (b) Schafer A, Huber C, Ahlrichs R. J Chem Phys 1994;100:5829.

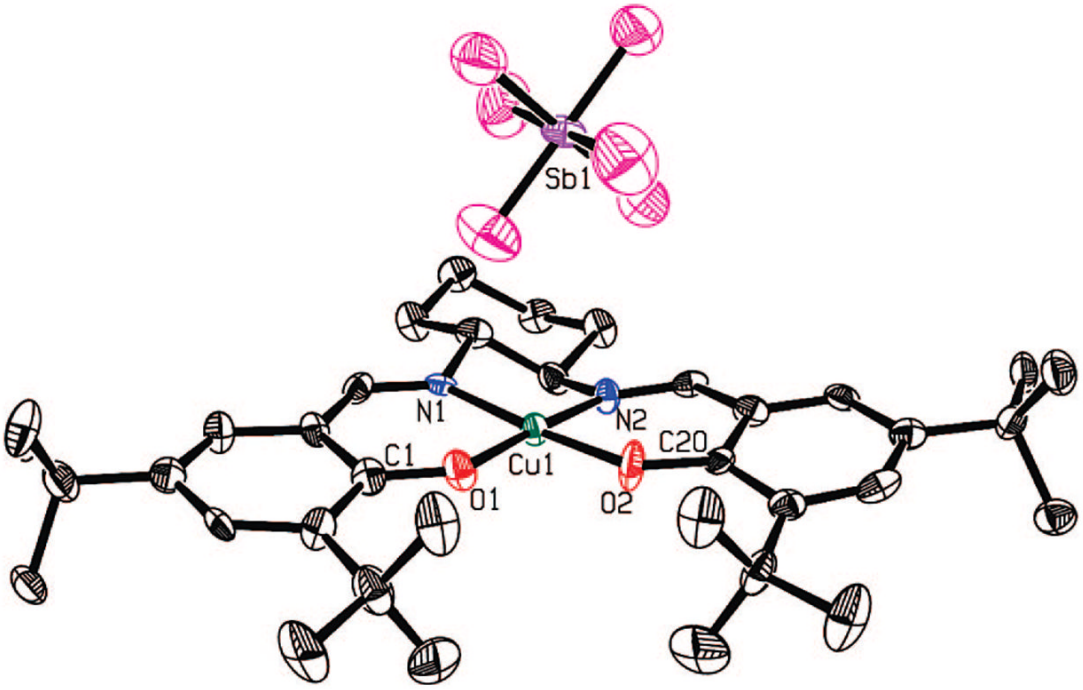

Figure 1.

ORTEP representation (50% probability) of [Cu**Sal**]$^{+}$SbF$_6^{-}$, excluding hydrogen atoms. Selected interatomic distances (Å) and angles (deg): Cu(1)–O(1), 1.831(6); Cu(1)–O(2), 1.838 (6); Cu(1)–N(1), 1.877(6); Cu(1)–N(2), 1.880(6); N(1)–C(7), 1.290(9); N(2)–C(14), 1.292 (10); O(1)–C(1), 1.317(10); O(2)–C(20), 1.317(9); O(1)–Cu(1)–O(2), 86.5(3); O(1)–Cu(1)–N (1), 94.3(3); O(2)–Cu(1)–N(2), 93.8(3); N(1)–Cu(1)–N(2), 85.7(3).

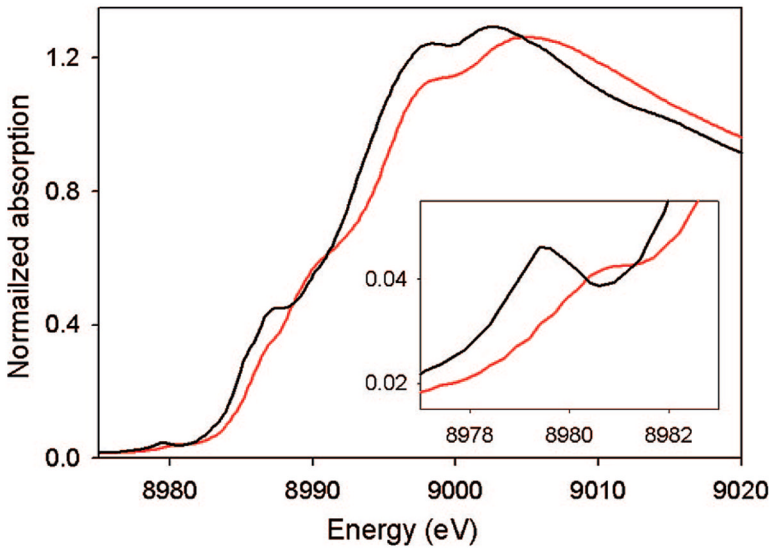

Figure 2.
Cu K-edges for Cu**Sal** (black) and [Cu**Sal**]$^{+}SbF_6^{-}$ (red). The inset amplifies the pre-edges (1s→3d transition).

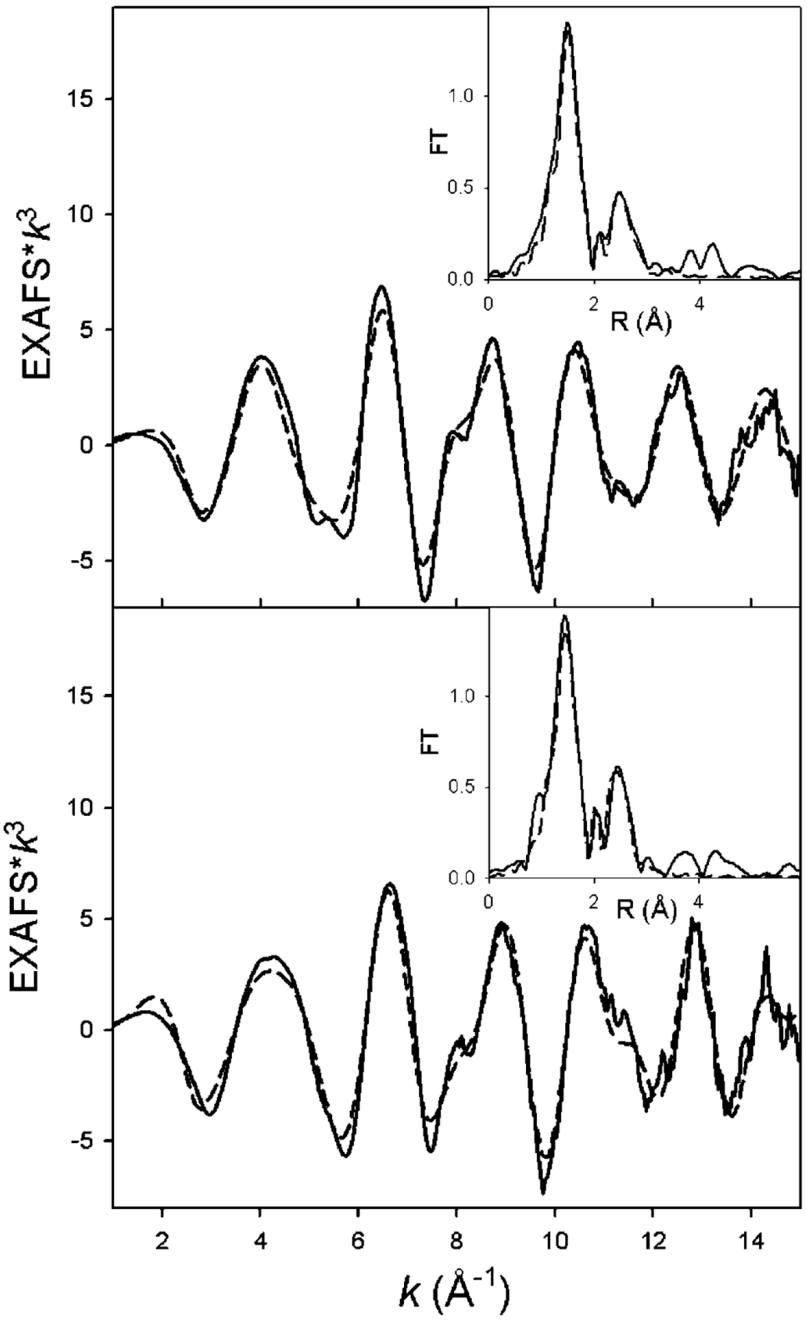

Figure 3.
Cu**Sal** (top) and [Cu**Sal**]$^{+}SbF_6^{-}$ (bottom) EXAFS data (solid lines) and fits (dashed lines). Insets: Fourier transforms (FT) and fits of the respective data.

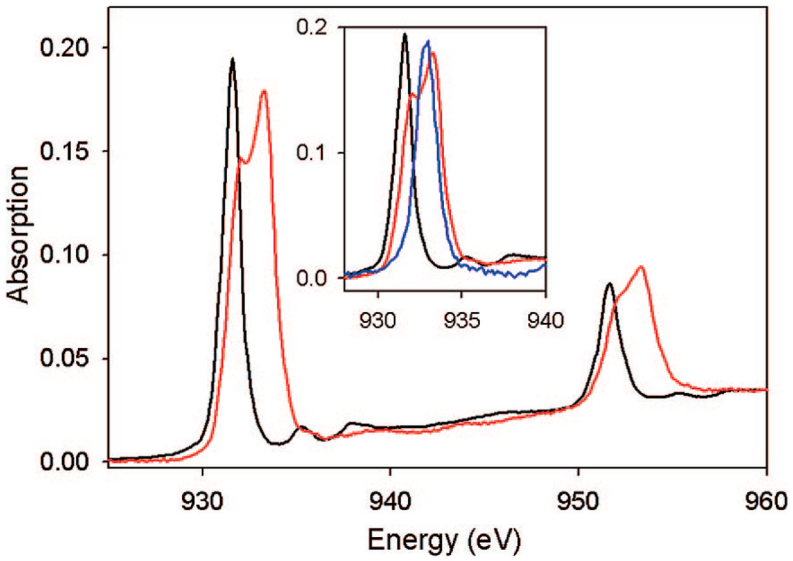

Figure 4.

Cu L-edge data of Cu**Sal** (black), and [Cu**Sal**]$^{+}$ (red). The two major features are the L_3-edge (ca. 930 eV, $2p_{3/2}\rightarrow 3d_{x^2-y^2}$) and the L_2-edge (ca. 950 eV, $2p_{1/2}\rightarrow 3d_{x^2-y^2}$). The inset shows the expanded L_3-edge region for Cu**Sal** (black), [Cu**Sal**]$^{+}$ (red), and $La_2Li_{0.5}Cu_{0.5}O_4$ (blue).

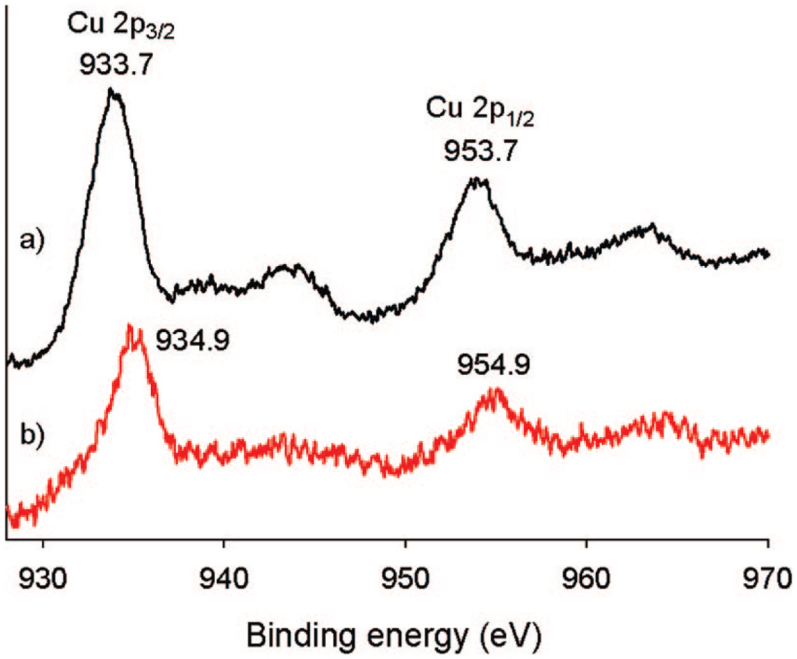

Figure 5.
X-ray photoelectron spectroscopy (XPS) data for Cu**Sal** (a) and [Cu**Sal**]$^{+}$ (b).

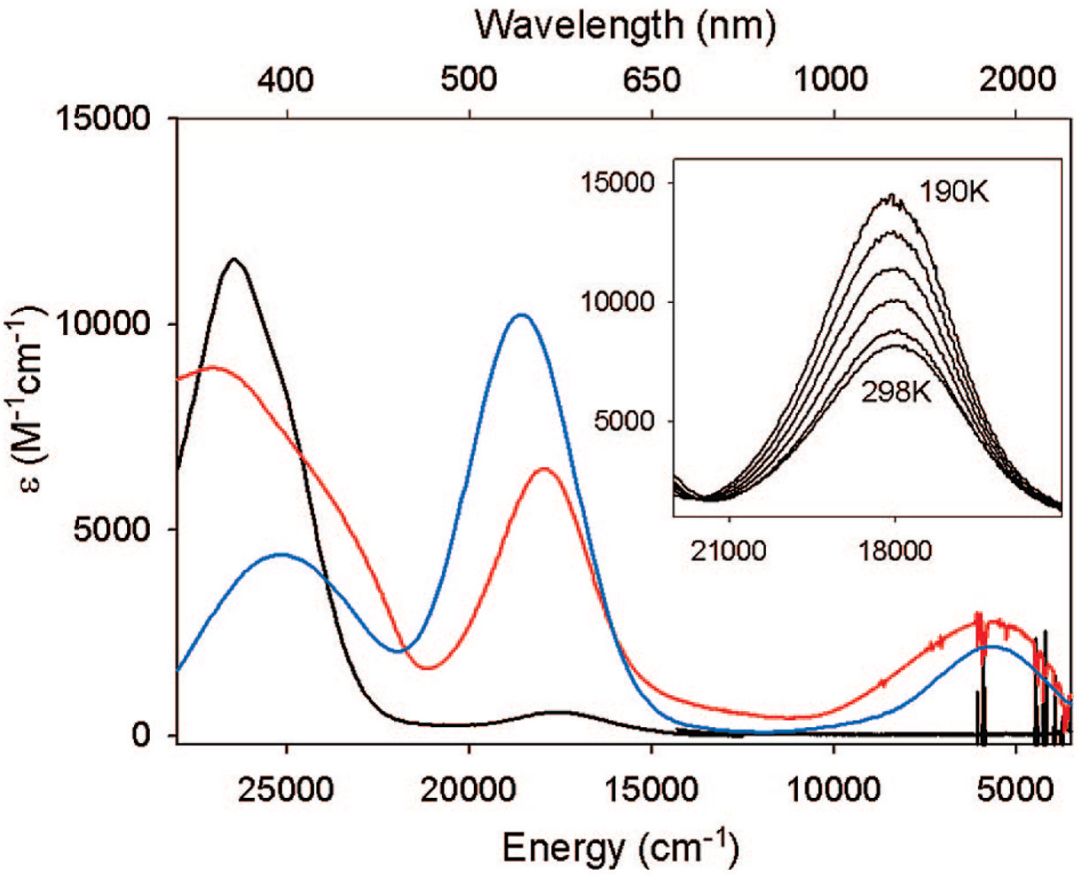

Figure 6.

Electronic spectra of 0.08 mM CH_2Cl_2 solutions of Cu**Sal** (black) and [Cu**Sal**]$^+SbF_6^-$ (red), and the calculated spectrum for singlet [Cu**Sal**]$^+$ (blue). Inset: Temperature dependence (298 →190 K) of the 18 000 cm^{-1} band.

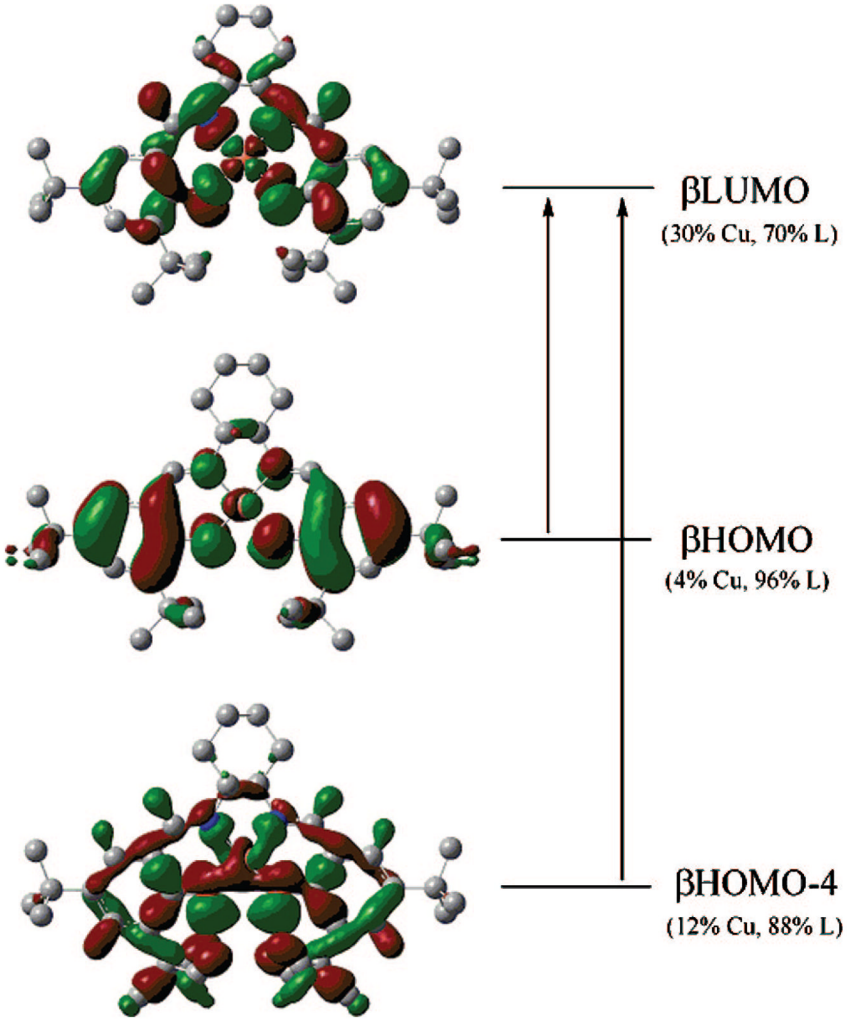

Figure 7.
TD-DFT assignment of the calculated transitions for the [Cu**Sal**]$^{+}$ singlet state at 18 600 (βHOMO-4 → βLUMO) and 5700 cm^{-1} (βHOMO → βLUMO). AOMIX decomposition of relevant MOs into constituent components is shown in parentheses.[42,43]

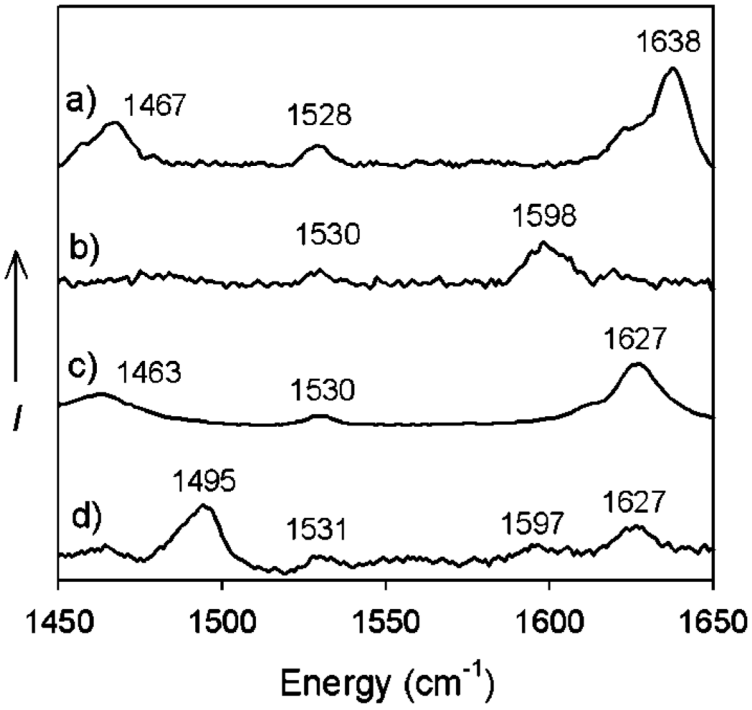

Figure 8.
Resonance Raman (rR) spectra of (a) Cu**Sal** and (b) [Cu**Sal**]$^{+}$ at 298 K, and of (c) Cu**Sal**$^{\mathbf{red}}$ and (d) [Cu**Sal**$^{\mathbf{red}}$]$^{+}$ at 213 K (λ_{ex} = 413 nm).

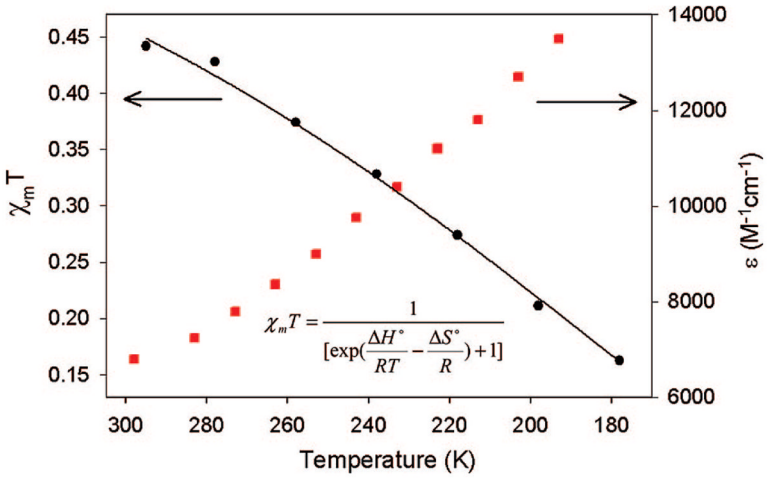

Figure 9.

Comparison of the VT solution susceptibility by ^{1}H NMR (black circles, CD_2Cl_2) and 18 000 cm^{-1} band intensity (red squares, CH_2Cl_2) for [Cu**Sal**]$^{+}SbF_6^{-}$. Fitting the susceptibility values (solid line) to the equation indicated affords thermodynamic parameters for the equilibrium ($\Delta H°$ = 1.1 ± 0.1 kcal mol^{-1}, $\Delta S°$ = 3.5 ± 0.1 cal K^{-1} mol^{-1}; R^2 = 0.998).

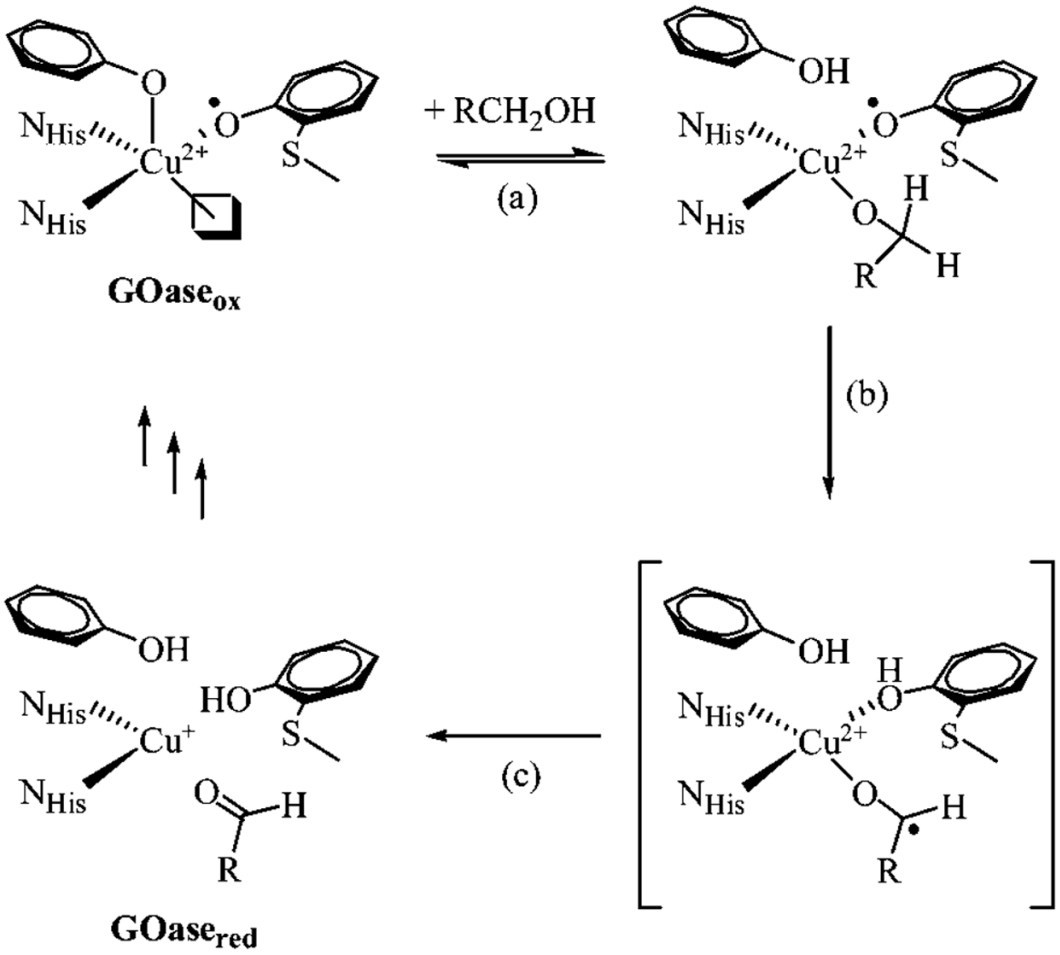

Scheme 1.

Consensus Mechanism for the Substrate-Oxidizing Half-Reaction of GOase[a]

[a] (a) Binding of the alcohol substrate to the exchangeable equatorial position on Cu and deprotonation by the axial tyrosine ligand. (b) Hydrogen atom abstraction from the substrate to the organic radical cofactor, forming a ketyl radical intermediate. (c) Electron transfer from the bound substrate to Cu and formation of the aldehyde product.

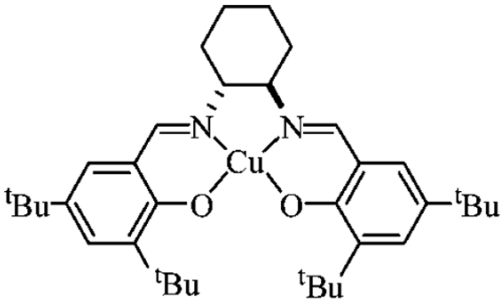

CuSal

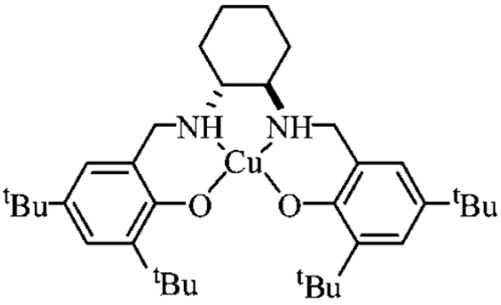

CuSal^{red}

Scheme 2.
Structures of Cu**Sal** and Cu**Sal**^{red}

$$\underset{\text{Cu(II)}-\text{phenoxyl (paramagnetic)}}{[\text{Cu(II)}\mathbf{Sal}^{\bullet}]^{+}} \rightleftarrows \underset{\text{Cu(III)}-\text{phenolate (diamagnetic)}}{[\text{Cu(III)}\mathbf{Sal}]^{+}}$$

(ferromagnetic coupling, $S = 1$) vs ($S = 0$)

Scheme 3.

Temperature-Dependent Equilibrium Process for [Cu**Sal**]$^{+}$ in Solution

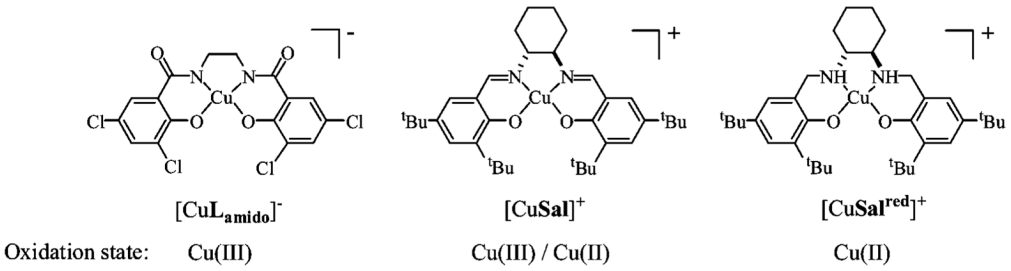

Scheme 4.

Metal Oxidation State Assignment for a Series of Square-Planar Cu-N_2O_2 Complexes[a]

[a] The amido ligand ($[\mathbf{L}_{amido}]^{4-}$) stabilizes the Cu(III) oxidation state,[27] while the tetrahydrosalen ligand ($[\mathbf{Sal}^{red}]^{2-}$) stabilizes the Cu(II) oxidation state. The salen ligand ($[\mathbf{Sal}]^{2-}$) is intermediate and is able to stabilize both Cu(II) and Cu(III) oxidation states.

Table 1

Selected Crystallographic Data for [Cu**Sal**]$^{+}$SbF$_6^{-}$

formula	$C_{36}H_{52}CuN_2O_2SbF_6 \cdot CH_2Cl_2$	α, deg	90
		β, deg	106.073(2)
fw	929.01	*γ*, deg	90
dimensions, mm^3	0.50 × 0.20 × 0.20	*λ*(Mo Kα)	0.71073
space group	C_2	*V*, Å^3	8224(2)
T, K	173(2)	*Z*	8
a, Å	37.646(6)	D_{calc}, g cm^{-3}	1.501
b, Å	9.892(2)	goodness of fit	1.050
c, Å	22.981(4)	$R1^a$ [$I > 2\theta(I)$]	0.0556
		w$R2^b$	0.1394

[a] $R1 = \Sigma||F_O| - F_C||/\Sigma|F_O|$.

[b] $wR2 = [\Sigma w(F_O^2 - F_C^2)^2/\Sigma w(F_O^2)^2]^{1/2}$.

Table 2

Comparison of the Experimental and Calculated Coordination Sphere Bond Lengths (Å) for Cu**Sal**[37] and [Cu**Sal**]$^+$

bond	CuSal (exp)	CuSal[a] (calc)	[CuSal]$^+$[b] (exp)	[CuSal]$^+$[a] (singlet calc)	[CuSal]$^+$[a] (triplet calc)
Cu1–O1	1.886(3)	1.896	1.841	1.840	1.892
Cu1–O2	1.887(3)				
Cu1–N1	1.915(4)	1.931	1.876	1.871	1.925
Cu1–N2	1.904(4)				

[a] Optimization results in a C_2-symmetric structure; see Experimental Section for details.

[b] Two [Cu**Sal**]$^+$ molecules exist in the unit cell; bond lengths are averages.

Table 3

Extended Charge Decomposition Analysis for M**Sal** and [M**Sal**]$^{+}$ (M = Ni, Cu)[a]

	α	β	total	α	β	total	|change|
		Cu**Sal** (*S* = 1/2)			[Cu(III)**Sal**]$^{+}$ (*S* = 0)		
L→Cu	+1.592	+2.646	+4.238	+3.418	+3.418	+6.836	2.598
Cu→L	−0.324	−0.320	−0.644	−0.536	−0.536	−1.072	0.428
net			+3.601			+5.770	
					[Cu(II)**Sal**$^{\bullet}$]$^{+}$ (*S* = 1)		
				+1.466	+3.510	+4.976	0.738
				−0.186	−1.218	−1.404	0.760
						+3.572	
		Ni**Sal** (*S* = 0)			[Ni(II)**Sal**$^{\bullet}$]$^{+}$ (*S* = 1/2)		
L→Ni	+2.342	+2.342	+4.684	+2.450	+2.828	+5.278	0.594
Ni→L	−0.534	−0.534	−1.068	−0.422	−1.300	−1.722	0.654
net			+3.616			+3.554	

[a] Values are reported for the α- and *β*-manifolds in units of electrons, with positive (+) values indicating ligand-to-metal electron donation.[42,44]

Table 4

Pre-edge Energies and Intensities and EXAFS Fitting for Cu**Sal** and [Cu**Sal**]$^{+}$

	pre-edge energy[a] (eV)	pre-edge intensity[a]	ligation	*R* (Å)[48]	σ^2 (Å^2)[48]
Cu**Sal**	8979.2(0.1)	3.1(0.1)	4 N/O	1.90	0.00266
[Cu**Sal**]$^{+}$	8980.2(0.1)	1.9(0.4)	4 N/O	1.86	0.00285

[a]Pre-edge energies and intensities are derived from fits of the data; see Experimental Section for details. Numbers in parentheses are standard deviations for the measured quantities.

Table 5

Cu L-Edge X-ray Absorption Spectroscopy Peak Energies (eV)

compound	**L_3-edge**	**L_2-edge**
$[C_4H_8N_3O]_2[CuCl_4]$[51]	931.0	951.0
$La_2Li_{0.5}Cu_{0.5}O_4$[51]	932.9	952.9
Cu**Sal**	931.6	951.7
[Cu**Sal**]$^+$[a]	931.8, 933.1	951.8, 953.2
[PPh_4][Cu-*N*, *N*′-*o*-phenylene-bis-(methylamide)][a26]	931.7, 933.7	951.9, 953.8

[a]Two observed peaks are due to facile photoreduction.[48]

Table 6

Predicted TD-DFT Transitions (Energies and Intensities) and Assignment for the Calculated Singlet and Triplet [Cu**Sal**]$^{+}$ Electronic States

complex	transition (MO number)[a]	energy (cm^{-1})	oscillator strength	assignment
[Cu(III)**Sal**]$^{+}$ (singlet)	βHOMO-4 (159) → βLUMO (164)	18 600	0.25	LMCT
	βHOMO (163) → βLUMO (164)	5 600	0.05	LMCT
[Cu(II)**Sal**$^{\bullet}$]$^{+}$ (triplet)	βHOMO-2 (160) → βLUMO+1 (164)	18 200	0.11	LMCT
	βHOMO-1 (161) → βLUMO+1 (164)			
	βHOMO (162) → βLUMO (163)	5 800	0.12	LLCT